Tectonics

RESEARCH ARTICLE
10.1029/2020TC006414

Key Points:

- Thermal modeling reveals two phases of rapid cooling and inferred exhumation after oblique collision
- The inversion to east-side-up tilting of the Northern Range is constrained to ~4 Ma
- Deformation and exhumation are consistent with the time-transgressive processes produced by a propagating lithospheric subduction-transform edge propagator fault

Supporting Information:

Supporting Information may be found in the online version of this article.

Correspondence to:

J. C. Arkle,
jennyarkle@augustana.edu

Citation:

Arkle, J. C., Weber, J., Enkelmann, E., Owen, L. A., Govers, R., Jess, S., et al. (2021). Exhumation of the coastal metamorphic belt above the subduction-to-transform transition, in the southeast Caribbean plate corner. *Tectonics*, *40*, e2020TC006414. https://doi.org/10.1029/2020TC006414

Received 3 JUL 2020
Accepted 27 JUL 2021

Exhumation of the Coastal Metamorphic Belt Above the Subduction-to-Transform Transition, in the Southeast Caribbean Plate Corner

Jeanette C. Arkle[1], John Weber[2], Eva Enkelmann[3], Lewis A. Owen[4], Rob Govers[5], Scott Jess[3], Chris Denison[6], Paul B. O'Sullivan[7], and Raymond A. Donelick[8]

[1]Department of Geology, Augustana College, Rock Island, IL, USA, [2]Department of Geology, Grand Valley State University, Allendale, MI, USA, [3]Department of Geoscience, University of Calgary, Calgary, AB, Canada, [4]Department of Marine, Earth, and Atmospheric Science, North Carolina State University, Raleigh, NC, USA, [5]Department of Earth Sciences, Utrecht University, Utrecht, The Netherlands, [6]Grand Rapids Community College, Grand Rapids, MI, USA, [7]GeoSep Services, Moscow, ID, USA, [8]Expert to Machine LLC, Viola, ID, USA

Abstract Plate corners that transition from subduction to transform motion can result in complex deformation. The southeastern corner of the Caribbean plate is a site where active westward subduction of the oceanic South American plate transitions to transform motion along continental South America. The Northern Range (Trinidad) and Paria (Venezuela) metamorphic mountains are located directly above this eastward propagating plate transition zone. We examined the exhumation history of the Northern Range and eastern Paria using apatite fission track (AFT) and apatite and zircon (U-Th)/He (AHe and ZHe, respectively) thermochronology on 21 bedrock samples. These samples yield ages of ~43–6 Ma (ZHe: aliquots), ~20–4 Ma (AFT: pooled) and ~5–2 Ma (AHe: aliquots). Along strike of the mountains, our new and published samples show a gradual eastward increase in age. Thermal modeling reveals two phases of rapid cooling and inferred exhumation that post-dates oblique collision and that migrated from west to east. We record an ~six-fold increase in cooling and exhumation between ~13–9 Ma in the Paria Peninsula and western Northern Range; a deceleration followed this rapid exhumation at ~7 and 5 Ma. Synchronous with the deceleration in the west, exhumation of the eastern Northern Range increased ~4 Ma. These post-collisional changes in exhumation constrain the inversion to east-side-up tilting of the Northern Range to ~4 Ma. We interpret the timing and pattern of exhumation since the mid-Miocene to be consistent with the time-transgressive processes produced by an eastward propagating lithospheric subduction-transform edge propagator fault.

1. Introduction

Regions where plate boundaries transition from subduction to transform motion are sites of complex deformational processes that are not well understood. Strain partitioning in such plate corners can vary considerably depending on plate geometry and other factors (e.g., Govers & Wortel, 2005; McCaffrey et al., 2007; Mann, 2007; Wallace et al., 2004). Much attention has been given to plate corners in which a converging plate is subducting and colliding along a concave boundary relative to the overriding plate. In this geometry, strain is concentrated at the plate corners and can form syntaxial regions characterized by bending of geologic structures, topography and focused exhumation (e.g., Arkle et al., 2013; Enkelmann et al., 2009; Zeitler et al., 2001). Studies in the syntaxes of southern Alaska and the Himalaya have shown that feedbacks between tectonics and surface processes can develop in syntaxial corners that result in some of the highest documented exhumation rates on Earth (e.g., Enkelmann et al., 2009; Koons et al., 2010; Zeitler et al., 2014). However, few studies exist that have explored exhumation along plate corners where subduction and collision of a plate occur along a convex boundary relative to the overriding plate. This geometry causes the subducting lithosphere to detach or tear away from the passive continental lithosphere beneath the surface transform boundary (Govers & Wortel, 2005; Wortel et al., 2009). The locus of active lithospheric tearing propagates toward the subduction zone and is referred to as a subduction-transform edge propagator (STEP; Govers & Wortel, 2005). Numerical models predict forearc vertical-axis block rotations along STEP margins (McCaffrey et al., 2007; Wallace et al., 2004) and kilometer-scale uplift and basin subsidence in the adjacent overriding plate (Clark, Zelt, et al., 2008; Govers & Wortel, 2005; Wortel et al., 2009). These crustal defor-

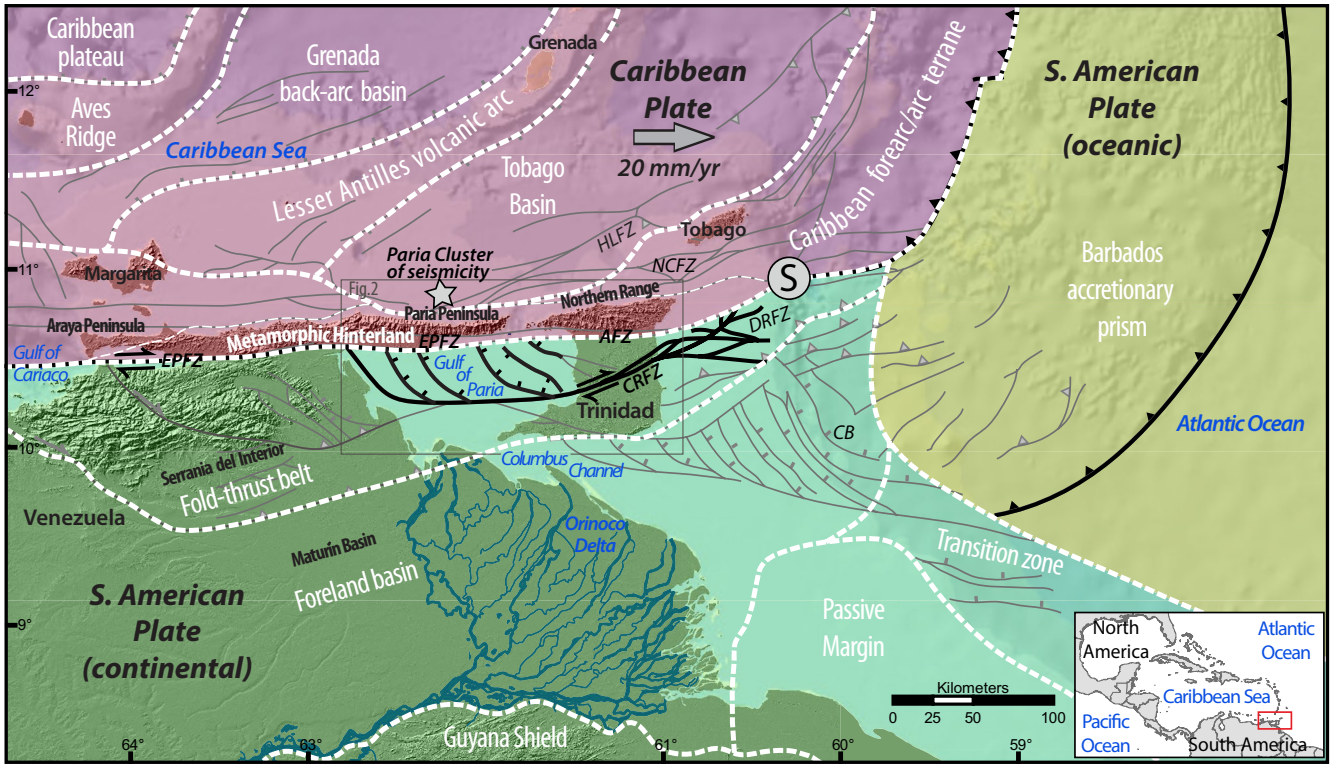

Figure 1. Tectonic setting of the southeast Caribbean showing major tectonic terranes and provinces (dashed white lines and white text) overlying topography (0.5-km-resolution digital elevation model from the U.S. Geological Survey), modified after Soto et al. (2011) and Speed and Smith-Horowitz (1998). Terranes of the Caribbean plate override the subducting oceanic portion of the South American plate (yellow shading) and move in a dextral sense relative to the continental portion of the South American plate (green shading). Major (bold black lines) and minor (thin gray lines) faults show relative motion where known, including thrust (teeth), normal (bar), and strike-slip (arrows) faults (after Garciacaro et al., 2011; Prentice et al., 2010; Soto et al., 2011). The Paria Cluster of seismicity (gray star; Russo & Speed, 1992) is located within the STEP fault zone and the inferred location of the STEP (gray circle with an "S") is shown. Relative Caribbean-South American plate motion from Weber, Dixon et al. (2001) and Weber et al., 2011. The gray box outlines the Paria Peninsula and Northern Range study area shown in Figure 2. AFZ–Arima fault zone; CB–Columbus Basin; CRFZ–Central Range fault zone; DRFZ–Darien Ridge fault zone; EPFZ–El Pilar fault zone; HLFZ–Hinge Line fault zone; NCFZ–North Coast fault zone.

mation patterns may occur over hundreds of kilometers in front of and behind a propagating STEP and are expected to exhibit specific temporal variations (Govers & Wortel, 2005; Wortel et al., 2009). Despite this general understanding, there is a lack of empirical data to test these models.

The southeast corner of the Lesser Antilles subduction zone is considered to be a STEP fault type-locality (Figure 1; Bilich et al., 2001; Govers & Wortel, 2005; Molnar & Sykes, 1969; Nijholt & Govers, 2015; Polonia et al., 2016; Russo et al., 1993; van Benthem et al., 2013; Wortel et al., 2009). The mountains of the Paria Peninsula in eastern Venezuela and Northern Range in Trinidad (and associate Maturin basin) currently straddle the largest negative continental Bouguer gravity anomaly on Earth (Russo & Speed, 1992). This gravity anomaly is attributed to mantle flow associated with the plate boundary transition from westward subduction of the oceanic South America plate to strike-slip motion between the continental South American and oceanic Caribbean plates (Figure 1; Alvarez, 2014; Clark, Levander, et al., 2008; Clark, Sobiesiak, et al., 2008; Clark, Zelt, et al., 2008; Miller et al., 2009; Russo et al., 1993). Eastward propagating detachment of oceanic South American lithosphere is proposed to accommodate subduction within a STEP fault zone along the positively buoyant continental South American lithosphere (e.g., Govers & Wortel, 2005; Molnar & Sykes, 1969; Clark, Levander, et al., 2008; Clark, Zelt, et al., 2008). STEP fault processes, such as asthenospheric flow, isostasy, and flexural bulging, are possible drivers of uplift and subsidence along this portion of the North American margin (Alvarez, 2014; Arkle, Owen, Weber, Caffee, & Hammer, 2017; Clark, Levander, et al., 2008; Clark, Sobiesiak, et al., 2008; Clark, Zelt, et al., 2008; Miller et al., 2009; van Benthem et al., 2013).

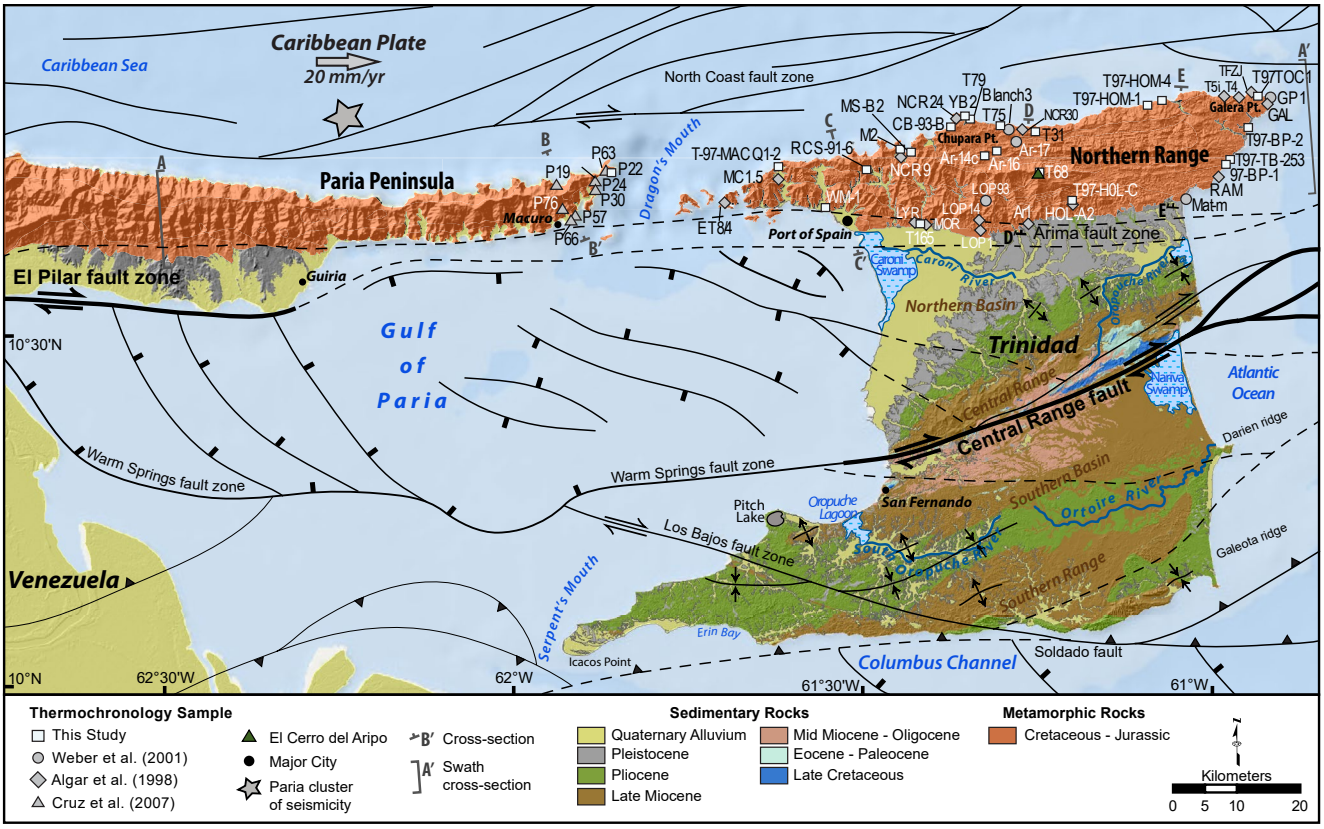

Figure 2. Geology of northeast Venezuela, the Gulf of Paria, and Trinidad on a 30-m-resolution digital elevation model showing bedrock thermochronology samples from this study and from Algar et al. (1998), Weber, Ferrill, and Roden-Tice (2001), and Cruz et al. (2007). Geology is generalized for the Paria Peninsula (Cruz et al., 2007) and Northern Range (de Verteuil et al., 2006) study area and south of the El Pilar and Arima fault zones (Soto et al., 2011). Structural data includes relative Caribbean-South American plate motion (Weber, Dixon, et al., 2001; Weber et al., 2011), the approximate location of the Paria Cluster of seismicity (star; Russo & Speed, 1992) along the STEP fault zone, and major faults (black lines) in the Gulf of Paria (Flinch et al., 1999), and Trinidad (Prentice et al., 2010; Soto et al., 2011). Locations of topographic and weather profiles are mapped and presented in Figures 3 and 4.

The mountains of the Paria Peninsula (Venezuela) and the Northern Range (Trinidad) sit directly above the plate boundary transition from subduction to transform motion (Figures 1 and 2). This region provides a unique setting to investigate the far- and near-field effects of the Caribbean plate corner transition. We use thermochronologic data to investigate the temporal and spatial patterns of rock uplift and exhumation above the STEP fault region. Our objectives are to (a) quantify the magnitude, rate, and timing of exhumation, and (b), evaluate the hypothesis that exhumation and deformation have been influenced by STEP fault activity.

2. Background

The mountains of the Paria Peninsula (Venezuela) and Northern Range (Trinidad) have experienced a protracted geologic history (Figure 2). Clastic protoliths of Paria Peninsula and Northern Range rocks were likely sourced from the Precambrian shield of South American; these and carbonate protoliths were likely deposited on a Jurassic-Cretaceous north-facing passive margin (e.g., Pindell et al., 1998). In the Miocene, the South American passive margin was contracted and tectonically thickened, and subducted beneath, and wedged over the Caribbean plate (Pindell et al., 2005; Roure et al., 1994; Russo & Speed, 1992; Summa et al., 2003). Metamorphism and exhumation of these mountains are widely attributed to oblique arc-continent collision from ~25–10 Ma (Algar et al., 1998; Babb & Mann, 1999; Foland et al., 1992; Pindell et al., 1998; Weber, Ferrill, & Roden-Tice, 2001). At ~10 Ma, the Caribbean-South American plate boundary stepped inboard to its current configuration and kinematics of transform motion (Figures 1 and 2; Algar & Pindell, 1993; Babb & Mann, 1999; Pindell et al., 1998).

The modern Caribbean-South American transform boundary strikes E-W on the El Pilar fault zone along the Paria Peninsula, steps right across the Gulf of Paria, and then strikes ~N72°E through central Trinidad as the Central Range Fault (Figure 2; Babb & Mann, 1999; Weber, Dixon, et al., 2001; Weber et al., 2011). The current relative Caribbean plate velocity is ~20 mm/yr toward ~N86°E in Trinidad (Weber, Dixon, et al., 2001; Weber et al., 2011). The development of the Gulf of Paria basin is related to pull-apart extension (Babb & Mann, 1999). This extension contributes to the modern subsidence of the eastern Paria Peninsula and western Northern Range and likely caused Quaternary east-side-up tilting of the Northern Range (Arkle, Owen, & Weber, 2017; Arkle, Owen, Weber, Caffee, & Hammer, 2017; Ritter & Weber, 2007; Weber, 2005). The majority of current Caribbean plate boundary dextral shear, ~12–15 mm/yr, is accommodated along the Central Range Fault in central Trinidad, which is ~30 km south of the Northern Range (Figures 1 and 2; Weber, Dixon, et al., 2001; Weber et al., 2011).

Dextral plate motion that occurs between the oceanic Caribbean and continental South American plates in Venezuela and Trinidad transitions eastward and offshore to west-directed subduction of the oceanic South American plate beneath the Caribbean plate (Figure 1; Algar & Pindell, 1993; Pindell et al., 1998; Russo & Speed, 1994; Soto et al., 2011; Speed et al., 1991). The intersection of the subduction megathrust and transform fault is the locus of active deep lithospheric tearing; this plate corner or edge is the site of an active STEP (Clark, Levander, et al., 2008; Clark, Sobiesiak, et al., 2008; Govers & Wortel, 2005). As lithospheric tearing propagates in a direction opposite to subduction, a STEP fault or fault zone develops in the wake (Baes et al., 2011; Özbakir et al., 2013). The southern Caribbean STEP fault zone is inferred from seismic tomography to be located along the margin of the continental South American lithosphere (Clark, Levander, et al., 2008; Clark, Sobiesiak, et al., 2008; Miller et al., 2009). The subducting oceanic lithosphere of the Atlantic slab (both the North and South American plates) is defined by a west-dipping Wadati-Benioff zone that extends to depths of ~300 km beneath the Lesser Antilles island arc and shallows eastward toward its surface trace near Barbados (Russo & Speed, 1994; Speed et al., 1991; Wadge & Shepherd, 1984). The southern termination of the Lesser Antilles trench is marked by the cessation of arc magmatism at the active subsea Kim'em Jenny volcano (near Grenada; ~12°N), and by a change in seismicity between ~12°–10°N at the South American slab edge (van Benthem et al., 2013). West of the South American slab edge seismicity reduces in frequency, occurs at shallow to intermediate depths, occurs as a nearly vertical plane, and has a significant dextral component of slip (Russo et al., 1993; Wadge & Shepherd, 1984). Shallow normal faulting to the E and NE of Trinidad makes up a broad field of horsts and grabens (Robertson & Burke, 1989; Russo et al., 1993; Weber et al., 2015) that could be related to plate flexure in a north-south direction ahead of the active STEP (Forsyth, 1975; Polonia et al., 2016). Behind the STEP (along Paria) downward plate flexure may reflect subsidence over the STEP-torn and sinking oceanic South American slab. Shallow dextral strike-slip faulting terminates or turns offshore east of Trinidad and, according to numerical models, can only occur up to the active subsurface STEP (Baes et al., 2011; Govers & Wortel, 2005). The location of the active STEP edge is defined at the intersection of shallow strike-slip faulting and the trench (Figure 1; circle with an "S"; after Nijholt & Govers, 2015). Offshore northern Venezuela, the Paria cluster of seismicity (star in Figure 1) is a source of frequent, deep (<200 km) earthquakes that occur within a narrow subvertical zone with a diameter of ~40 km (Clark, Sobiesiak, et al., 2008). This seismicity may be associated with the tearing process between the sinking slab in the north and the South America lithosphere in the south.

Directly above the proposed STEP fault, the east-trending metamorphic rock and coastal mountains that we study reach elevations of only ~1 km above mean sea level and form a relatively narrow hinterland exposure (~15 km wide). Relict ammonites reported from the Maraval assemblage in the Northern Range constrain some of the protolith depositional ages to be ~150–67 Ma (Saunders, 1972). Metamorphic grade decreases eastward from greenschist to sub-greenschist grade (Figure 2; Frey et al., 1988; Gonzá lez de Juana et al., 1972). Muscovite $^{40}Ar/^{39}Ar$ ages indicate metamorphism at ~25–30 Ma in the Paria Peninsula and the western Northern Range (Foland et al., 1992; Speed et al., 1997). Geothermometry data indicate that rocks in the eastern Northern Range did not experience temperatures >200–250°C (Weber, Ferrill, & Roden-Tice, 2001). Eastward decreases of metamorphic age and grade are inferred to be related to the initial collision of the southeast-directed Caribbean plate front, with compression occurring in front of the advancing plate (e.g., Pindell & Kennan, 2009). Previous thermochronology studies found zircon and apatite fission track ages are fully reset in the Paria Peninsula and western Northern Range (Algar et al., 1998; Cruz et al., 2007; Weber, Ferrill, & Roden-Tice, 2001). In contrast, unreset zircon fission track (ZFT) ages are

located almost exclusively in the eastern Northern Range, along with three partially reset samples interpreted to be dispersed due to counting on heavily abraded grains and/or annealing kinetics (Algar et al., 1998). These fission track ages were interpreted to indicate asymmetric exhumation, with exhumation decreasing eastward (Algar et al., 1998; Frey et al., 1988; Weber, Ferrill, & Roden-Tice, 2001).

Geomorphic patterns and estimates of surface uplift rates from Quaternary marine terraces indicate that the locus of uplift and exhumation in the west inverted to east-side-up tilting of the Northern Range post-collision (Ritter & Weber, 2007; Weber, 2005). ^{10}Be erosion rate data and geomorphic analyses indicate this inversion initiated during the mid-Pliocene to the Holocene and that tectonic tilting was the dominant driver of inversion and east-side-up tilting of the Northern Range (Arkle, Owen, Weber, Caffee, & Hammer, 2017). The along-strike transition from surface subsidence in the west to uplifted topography in the east could alternatively correspond with STEP-related processes and be related to lithospheric flexure at the plate corner. Based on the spatial correlation of topography and the timing of the tectonic inversion, post-collision tectonic tilting of the Northern Range has recently been interpreted to be consistent with deep subsurface lithospheric detachment processes and associated crustal extension (Arkle, Owen, Weber, Caffee, & Hammer, 2017).

3. Methods

In this study, we use apatite and zircon (U-Th)/He (AHe and ZHe, respectively) and apatite fission track (AFT) thermochronometers to evaluate bedrock cooling and histories of the Northern Range and eastern Paria Peninsula. Thermochronology utilizes the preservation of radiogenic decay products in a mineral. Fission tracks and helium are thermally sensitive, and retention occurs through a range of temperatures referred to as the partial annealing zone (PAZ) for fission track (e.g., Green et al., 1986) and the partial retention zone (PRZ) for the (U–Th)/He systems (e.g., Farley, 2000; Reiners, 2005). The retention of radiogenic products begins at a specific temperature within the PAZ or PRZ called a closure temperature (T_C), which varies with cooling rate and mineral properties such as grain size and composition (Dodson, 1973; Farley, 2000; Reiners, 2005). Temperatures higher than a mineral's closure temperature can cause annealing of fission tracks or diffusive loss of helium and result in a reset cooling age (e.g., Brandon et al., 1998; Farley, 2000; Flowers et al., 2009). In this study, we analyze thermochronologic systems with closure temperatures that range from ~55–75°C (AHe; Farley, 2000), ~100–120°C (AFT; Green et al., 1986), ~160–200°C (ZHe; Reiners, 2005), and ~210–300°C (ZFT; Brandon et al., 1998).

3.1. Sampling

Twenty-one bedrock samples, weighing 2–8 kg, were collected along an ~160-km-long transect, which is sub-parallel to current relative Caribbean-South American plate motion (Figures 2 and 3). Eleven samples are from the western Northern Range and nine samples are from the eastern Northern Range. One bedrock sample from the Paria Peninsula was collected near the published data sites of Cruz et al. (2007; Figure 2). Since our study focuses on investigating exhumation related to the Caribbean plate's eastward motion, most samples were collected between sea level and ~100 m, with only one high-elevation sample collected from a peak (El Cerro del Aripo) at ~935 m. Most of the samples are from coarse-grained metasandstone, others include those from schist, metacarbonate, phyllite, and quartzite.

3.2. Analytical Techniques

Apatite and zircon grains were extracted from samples for (U-Th)/He and fission track analysis with separation techniques detailed in the supplemental text (e.g., Reiners & Farley, 2001). Raw apatite and zircon ages were corrected for alpha ejection effects (Ft correction) following the methods of Farley (2002). The reproducibility of single grain ages and the effects of possible radiation damage were evaluated with grain size and the effective uranium (eU) concentration, which is a proxy for radiation damage (Ault et al., 2019; Flowers et al., 2009). We consider ages to be reproducible when the 1σ is <20% of the mean age (Flowers et al., 2009). For dispersed aliquots with possible size or eU age controls, the range of single grain ages is reported for a sample (Ault et al., 2019; Flowers et al., 2009). We calculated the arithmetic mean (U-Th)/He age only for samples with more than two reproducible single grain ages (e.g., Fukuda et al., 2020).

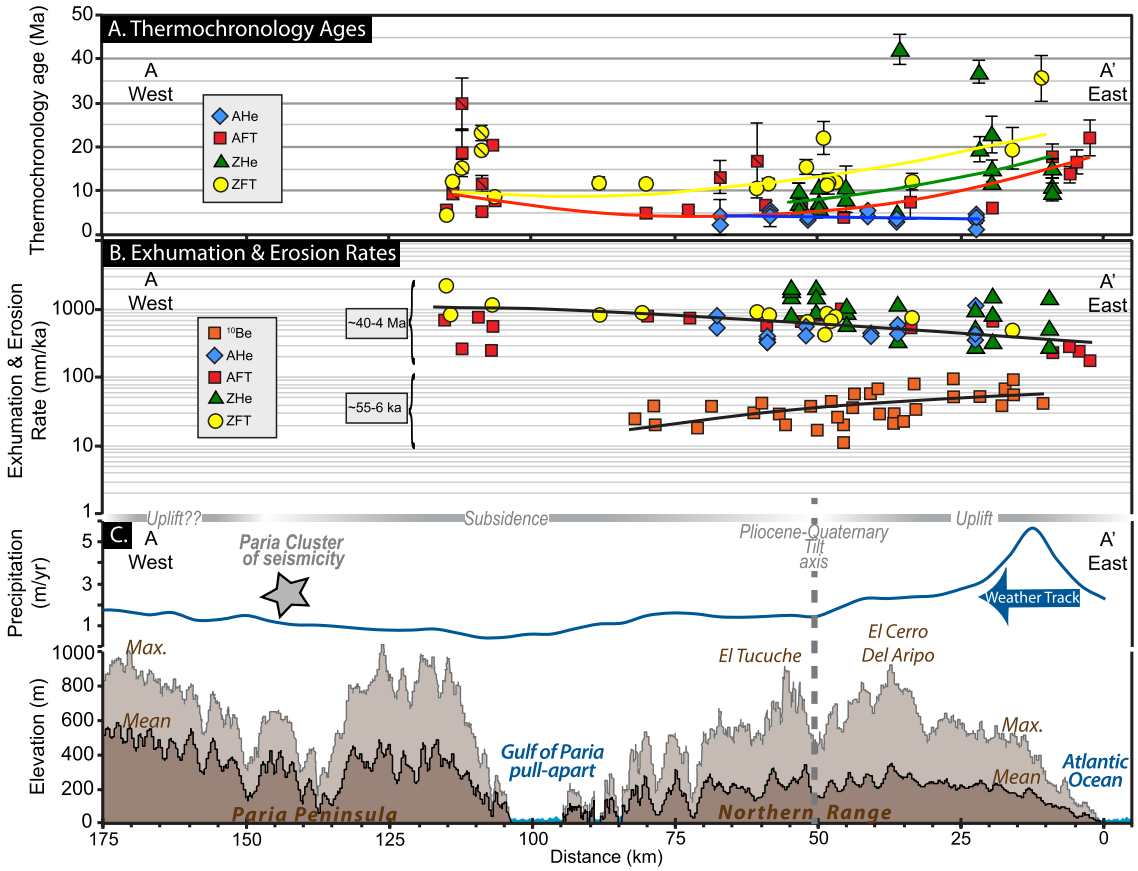

Figure 3. East-west profiles across the Northern Range in Trinidad, Gulf of Paria, and eastern Paria Peninsula in Venezuela correlated to location above the topography. (a) Thermochronology data apatite and zircon (U-Th)/He (AHe and ZHe data are single grain ages) plotted with (±1σ) and (b) exhumation and erosion rates derived over multiple time scales. Thermochronology data are from this study, Algar et al. (1998), Weber, Ferrill, and Roden-Tice (2001), and Cruz et al. (2007) and ^{10}Be erosion rate data are from Arkle, Owen, Weber, Caffee, and Hammer (2017). Fission track samples that failed the chi-squared test or are partially reset have a line on the symbol and unreset zircon fission track (ZFT) ages are not shown here. Best-fit linear (black lines) and polynomial regressions (color corresponds to each thermochronometer) show the general data trends. Thermochronology data integrate over time periods of ~40–4 Ma and ^{10}Be data integrate over the last ~55–6 ka (Arkle, Owen, Weber, Caffee, & Hammer, 2017). (c) Swath profiles of the mean (dark brown) and maximum (light brown) topography and average annual precipitation rates (Hijmans et al., 2005) over the region. Location of profiles are shown in Figure 2.

Apatite fission track ages were determined from spontaneous fission track densities in individual apatite grains and relative uranium concentrations using laser-ablation–inductively coupled plasma–mass spectrometry (LA-ICP-MS; Donelick et al., 2005). Dpar was measured on most grains from all dated samples to assess annealing kinetics. The chi-squared test [$P(\chi^2)$] was used to determine the statistical probability that a population of ages is drawn from a single age population with a normal distribution (e.g., Galbraith, 1990).

3.3. Thermal History Modeling

Time-temperature (*t-T*) histories were modeled using the program QTQt (Gallagher, 2012) with our new and published thermochronology data (Algar et al., 1998; Cruz et al., 2007; Weber, Ferrill, & Roden-Tice, 2001). Thermal histories in QTQt were calculated using a Bayesian Transdimensional Markov Chain Monte Carlo inversion, which computes 200,000 possible thermal histories and continually assesses each path with a log-likelihood function by applying an acceptance criterion that attempts to improve predictions (Gallagher, 2012). An expected model is produced from the weighted average of the final probability distribution and includes the associated uncertainty for the samples with the coldest (highest elevation) and hottest (lowest elevation) thermal histories (Gallagher, 2012). This modeling approach allows for the joint inversion of multiple thermochronometers and multiple samples, and can determine a single thermal history of samples located in different structural positions and varying elevations (Gallagher, 2012).

Our multiple thermochronometer and multiple sample thermal modeling approach was based on exploring thermal histories within three structural-metamorphic regions (eastern Paria, and the western and eastern Northern Range), which are shown in Figure 5. Distinct changes in metamorphic grade and thermochronology ages occur across the Gulf of Paria and along a N-S zone near the center of the Northern Range (hashed line, Figure 5); this includes the occurrence of unreset ZFT ages located almost exclusively in the east, which separates the western from eastern Northern Range. There is also a major difference across this N-S zone in the Northern Range of quartz and calcite geothermometry (Weber, Ferrill, & Roden-Tice, 2001), and changes defined by ^{10}Be erosion data and geomorphology (Arkle, Owen, & Weber, 2017; Arkle, Owen, Weber, Caffee, & Hammer, 2017). Within a region, the thermochronology ages, metamorphic grade, and lithologic character are similar, yet discrete faults or other structures that dissect the mountains are largely unknown (Algar et al., 1998; Foland et al., 1992; Weber, Ferrill, & Roden-Tice, 2001). Thus, we chose to focus the thermal modeling within these structural regions as a whole, in order to characterize the general exhumation trends across the study area. In the case of low model confidence or possible thermal complexities, models were attempted with single samples and groupings of samples within a region.

Only aliquots with reproducible (U-Th)/He ages or dispersed ages with possible size or eU age controls were used in the models. Possible effects of radiation damage were accounted for using the model calibrations of Flowers et al. (2009) and Guenthner et al. (2013), and by using single grain AHe and ZHe data in each model, while error resampling was used to restrict the influence of grains that did not conform to the rest of the input data. Thermal models included fission track ages only for samples with >10 measured track lengths, associated Dpar and confined track length distributions. The annealing models of Ketcham et al. (2007) and Tagami et al. (1998) were used for the AFT and ZFT systems, respectively. AFT data from this study are presented in Tables S3–S6. Single grain fission track is not available for the Northern Range (no ZFT tracks or single grain ages) or Paria Peninsula (no AFT and ZFT tracks; Cruz et al., 2007). We follow the reporting protocol of Flowers et al. (2015) by outlining the thermal history model inputs, parameters, and geologic constraints in Table S7.

In the Paria Peninsula and western Northern Range, a *t-T* constraint was set based on ^{40}Ar/^{39}Ar metamorphic ages of ~30–25 Ma (Foland et al., 1992; Speed et al., 1997). There is currently no equivalent data on the metamorphic history of the eastern Northern Range, so to obtain data-driven results no constraints were included for that region. We do not have other geologic information on the depths/temperatures experienced by the samples after metamorphism in the mid-Miocene, so a broad box was used in all models to allow the program to freely search for acceptable solutions within a wide space. For all models the end constraint was set to current surface temperatures (25 ± 5°C) for the present. To assess if user-defined constraints influenced the shape of the cooling history, we explored *t-T* histories for Paria and the western Northern range without using any constraint boxes to avoid forcing paths into a narrow space.

4. Results and Data Analysis

4.1. Zircon (U-Th)/He Ages

Seven samples from the Northern Range yield 21 single grain ZHe ages (Tables 1 and S1). All four samples collected from the eastern Northern Range (T68, T97-BP-1, T97-HOM-1, and T97-HOM-4) display intrasample dispersion with an average $1\sigma > 47\%$. Two of these samples (T68 and T97-HOM-1) each yield one single grain age that exceeds the depositional age of the rock and are considered outliers. Excluding these two single-grain ages, the aliquots for all four dispersed samples show weak correlation between single-grain ages and grain size (Figure S1). However, correlation between aliquots and eU, similar to relationships described by Guenthner et al. (2013), might explain the age dispersion (Figure S1). Zoning of parent elements within zircon grains is common and could account for the spread of ages, but it was not tested for (Flowers et al., 2009). Another possibility is that the zircons may retain pre-depositional ^{4}He and/or may have spent a substantial amount of time within the PRZ before exhumation, resulting in radiation damage. Radiation damage is likely given that several published ZFT and AFT samples from the eastern Northern Range yielded partially reset ages (Algar et al., 1998; Weber, Ferrill, & Roden-Tice, 2001). Since these dispersed aliquots have possible eU controls, and thus, may contain important information regarding the thermal history of rock (e.g., Zapata et al., 2019), we include them in the thermal models and report the range of single-grain ages for samples from the eastern Northern Range, which is 5.8 ± 1.3 to 43.8 ± 5.0 Ma. Three samples from

Tectonics

10.1029/2020TC006414

Table 1
Summary of Bedrock Thermochornology Data From the Northern Range, Trinidad and Eastern Paria Penisula, Venezula

					Zircon fission track					Zircon helium				Apatite fission track						Apatite helium			
Sample ID	Lithology	Elv. (m)	Lat. (°N)[a]	Long. (°W)[a]	ZFT age (Ma)[b]			*n*	*P* (χ^2) (%)	ZHe age (Ma)[b]			*n*	AFT age (Ma)[b]			*n*	Dpar (μm)	*P* (χ^2) (%)	AHe age (Ma)[b]			*n*
Eastern Northern Range																							
T31	Metasand	52	10.788	−61.250																5.1	±	0.3	3
T68	Metaschist	935	10.730	−61.243						5.9–43.8	±	1.3–5.0	2							2.9–3.3	±	0.9–1.1	2
T97-H0L-C	Metaschist	191	10.689	−61.197										7.3	±	3.7	3	1.48	99				
T-97-BP-2	Metasand	14	10.746	−60.970										17.5	±	3.3	3	1.56	82				
T97-TOC-1	Metasand	39	10.836	−60.929										16.6	±	2.8	10	1.63	43				
T97-HOM-4	Metasand	30	10.831	−61.067						9.9–23.2	±	1.1–3.1	3	6.1	±	0.6	36	1.55	11				
T-97-TB-253	Metasand	7	10.792	−60.943										13.7	±	2	9	1.76	2.1				
T97-BP-1	Metasand	24	10.746	−60.970						8.7–15.4	±	1.0–1.9	3										
T97-HOM-1	Metasand	39	10.824	−61.088						18.9–36.9	±	1.6–2.6	2							3.4	±	0.8	4
Mat-m[c]	Metasand	18	10.690	−61.033	19.4	±	3.1	13	1.2														
GP-1[c]	Metasand	6	10.834	−60.911	83.7	±	14	17	1.3					22	±	4	7		5.3				
HOL-A2[d]	Metaschist	169	10.684	−61.196	14.2	±	1.0	12	0.4														
RAM[d]	Metaschist	8	10.722	−60.987	38.8	±	4.6	7	0														
NCR 30[d]	Metasand	56	10.795	−60.271	271.0	±	42	4	100														
GAL[d]	Metasand	20	10.829	−60.921	116.0	±	9.0	10	0.1														
T4[d]	Metasand	5	10.833	−60.958	121.0	±	7.2	11	9														
T5i[d]	Metasand	52	10.836	−60.979	202.0	±	16	9	3														
AR1[d]	Metasand	70	10.652	−60.257	60.6	±	4.1	8	0														
TFZJ[d]	Metasand	0	10.840	−60.944	61.1	±	4.5	8	0														
Ar-17[c]	Metasand	120	10.778	−60.285	172.3	±	34	14	93.4														
Western Northern Range																							
T75	Metaschist	0	10.796	−61.299						8.0	±	0.4	3										
T79	Metacarbonate	0	10.806	−61.343						7.4	±	0.6	3							4.0–2.8	±	0.9–1.3	2
T97MACQ1-2	Quartzite	33	10.739	−61.619										4.9	±	1.2	20	1.37	99				
WM-1	Metasand	11	10.681	−61.552										5.5	±	0.7	37	1.46	100				
MS-B2	Quartzite	23	10.759	−61.428										6.7	±	1	39	1.48	98.4				
CB-93-B	Metasand	67	10.795	−61.371										6.1	±	0.8	36	1.46	99				
YB-2	Metasand	9	10.807	−61.346										5.1	±	0.7	10	1.61	0.53				
Ar-16	Metasand	111	10.761	−61.305										4	±	0.5	10	1.57	26.3				
RCS-91-6	Quartzite	365	10.734	−61.492										13.1	±	3.8	36	1.66	0.65	2.2–4.7	±	5.7–7.2	2
Ar-14c	Metasand	261	10.754	−61.322						8.0	±	0.5	3										

Tectonics

10.1029/2020TC006414

Table 1
Continued

Sample ID	Lithology	Elv. (m)	Lat. (°N)[a]	Long. (°W)[a]	Zircon fission track ZFT age (Ma)[b]			n	P (χ^2) (%)	Zircon helium ZHe age (Ma)[b]	n	Apatite fission track AFT age (Ma)[b]			n	Dpar (μm)	P (χ^2) (%)	Apatite helium AHe age (Ma)[b]			n
LOP-93[c]	Metasand	234	10.689	−61.321	12	±	1.5	20	1.9												
Blanch-3[c]	Metasand	37	10.803	−61.336	22.1	±	3.8	8	99.3												
LYR[d]	Metasand	89	10.659	−61.424	11.9	±	1	11	30												
NCR24[d]	Metasand	45	10.807	−61.363	15.4	±	1.2	10	29												
LOP1[d]	Metasand	134	10.648	−61.329	11.8	±	1.3	8	100												
LOP14[d]	Metasand	154	10.661	−61.331	11.3	±	1.3	9	6												
MC1.5[d]	Quartzite	51	10.722	−61.619	11.7	±	0.9	11	4												
NCR9[d]	Quartzite	22	10.760	−61.443	10.7	±	0.6	17	31												
ET8/4[d]	Quartzite	2	10.688	−61.696	11.9	±	1.4	6	75												
T165	Metasand	75	10.657	−61.423															5.5	±	0.4	3
MOR[d]	Metasand	33	10.654	−61.403	205	±	18.1	8	0												
Eastern Paria Peninsula																					
PP-022	Dragon Gneiss	180	10.733	−61.867								20.3	±	0.9	40	1.50	52.8				
PP-019[e]	Schist and quartzite	0	10.715	−61.938	4.7	±	0.9	5	18.1			5.7	±	0.9	20		37				
PP-024[e]	Gneiss	0	10.719	−61.883	19.3	±	0.8	20	1			5.2	±	0.8	20		32				
PP-063[e]	Gneiss	0	10.732	−61.863	8.7	±	0.7	5	17.3			7.6	±	0.8	21		11.6				
PP-030[e]	Schist and quartzite	60	10.708	−61.882	23.0	±	1.5	11	1			11.6	±	1.9	20		1.1				
PP-076[e]	Schist and quartzite	100	10.679	−61.929	12.3	±	0.6	20	14.7			9.3	±	1.4	20		2.4				
PP-057[e]	Schist and marble	165	10.671	−61.909								29.9	±	5.9	8		2.8				
PP-066[e]	Schist and marble	0	10.662	−61.915	15.4	±	0.7	20	1			18.8	±	4.8	8		81.5				

Note. *n* is the number of grains analyzed for fission-track or (U-Th)/He analysis. Dpar is the etch pit diameter parallel to crystallographic c axis. *P* (χ^2) is the Chi-squared probability percent. [a]Sample datum are reported in WGS 84. [b]Mean age or age range is reported based on criteria described in the text and from analytical data (Tables S1 and S2). [c]Age from Weber, Ferrill, and Roden-Tice (2001). [d]Age from Algar et al. (1998). [e]Age from Cruz et al. (2007).

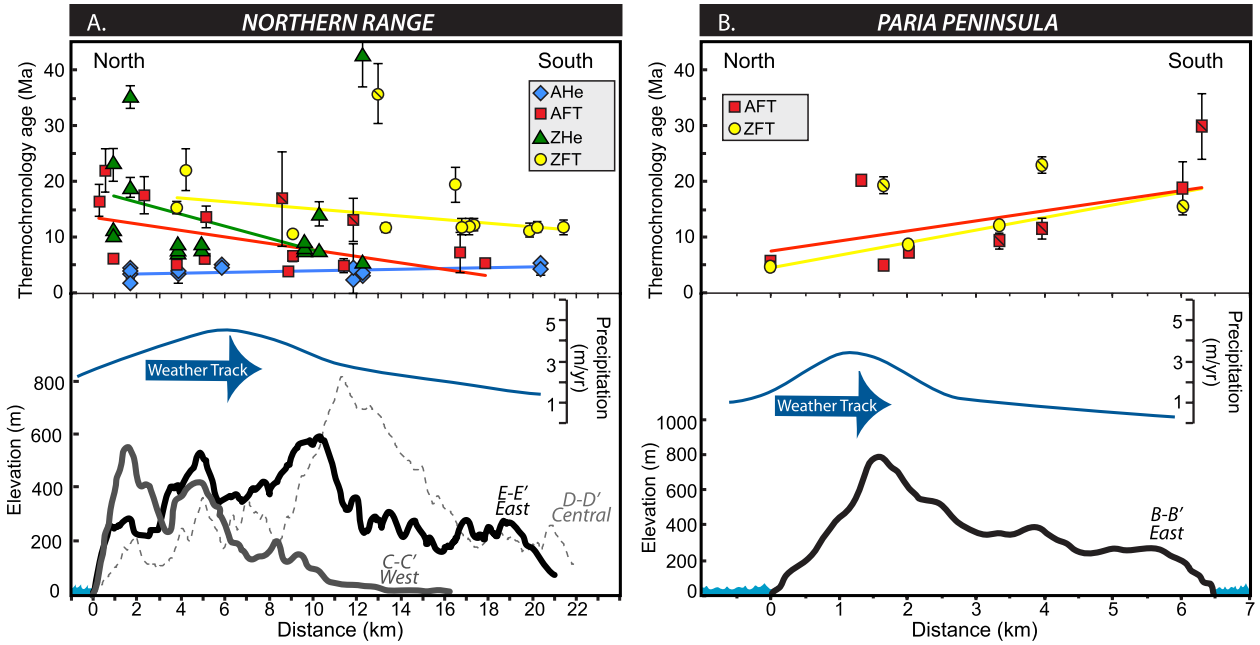

Figure 4. (a) North-south profiles across the Northern Range in Trinidad and (b) eastern Paria Peninsula in Venezuela. Upper panels show thermochronology single grain apatite and zircon (U-Th)/He (AHe and ZHe) ages (±1σ) and apatite and zircon fission track (AFT and ZFT) data (±1σ) (this study; Algar et al., 1998; Cruz et al., 2007; Weber, Ferrill, & Roden-Tice, 2001) with the best-fit linear regressions (color corresponds to each thermochronometer) to show the general data trends. Fission track samples that failed the chi-squared test or that are partially reset have a line on the symbol and unreset ZFT ages are not shown here. Lower panels show average annual precipitation rates (Hijmans et al., 2005) and topographic profiles (locations shown in Figure 2) of the eastern Paria Peninsula (B-B'; black) and the eastern (E-E'; black), central (D-D'; dashed), and western (C-C'; gray) Northern Range.

the western Northern Range yield single-grain ZHe ages that reproduce well (average 1σ is 10%) and mean ages range from 7.4 ± 1.1 to 8.0 ± 0.9 Ma (Table S1; Figures 3, 4, and S1).

4.2. Apatite Fission Track Ages

Nine of the 12 samples from the Northern Range yield AFT pooled ages that range from 4.0 ± 0.5 to 17.5 ± 3.3 Ma. The new sample from eastern Paria gave a pooled age of 20.3 ± 0.9 Ma (Tables 1, S3–S5 and Figures 3 and 4). Single-grain age distributions for 10 samples display $P(\chi^2)$ typically >44%, indicating one age population is present in these samples and the pooled AFT ages are reported (Galbraith, 1990). Three samples (T-97-TB-253, YB-2, and RCS91-6) failed the $P(\chi^2)$ test (<5%), indicating a poly-modal distribution of single-grain ages. Given these samples are from metasedimentary rocks, the wide spread of single grain ages may be due to apatite grains with compositional differences. Differential annealing can occur in grains with different compositions, particularly with long-term residence within the PAZ, and can yield a wide-spread in single grain ages (Donelick et al., 2005; Galbraith, 1990). The samples that failed the $P(\chi^2)$ test have a wide range of kinetic annealing parameters (Dpar values); Dpar for T-97-TB-253 ranges from 1.19 to 2.27 μm, Dpar for YB-2 ranges from 1.30 to 1.94 μm, and Dpar for RCS91-6 ranges from 1.33 to 2.41 μm (Tables S4 and S6). The average sample Dpar, excluding samples that failed the $P(\chi^2)$ test, varies from ~1.0 to ~2.5 μm, and shows no systematic variation or positive correlation between samples. Track lengths from the Northern Range average 13.69 ± 0.93 μm; in the east the average is 13.71 ± 0.84 μm and in the west the average is 13.68 ± 0.99 μm.

4.3. Apatite (U-Th)/He Ages

Six samples from the Northern Range yield 21 single grain AHe ages (Tables 1 and S2). Three samples display intrasample dispersion (1σ > 20% of the mean age; Figure S2). In sample T97-HOM-1 there is one outlier single grain AHe age (with respect to four reproducible single grain ages) that is considerably smaller (dimensional mass = 0.19) than the intrasample aliquots and is considered an outlier (Table S2 and Figure S2).

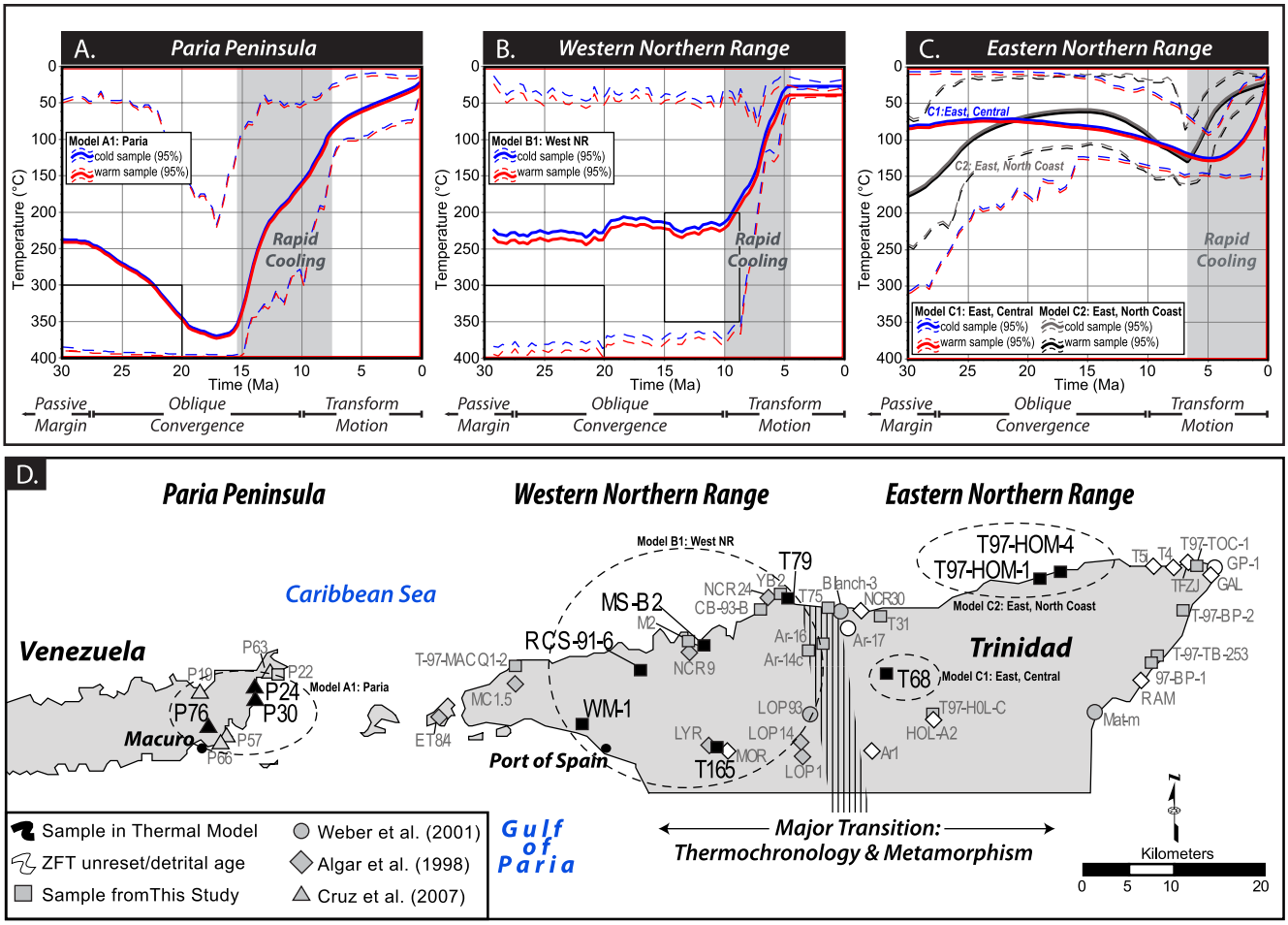

Figure 5. (a–c) Thermal histories derived from joint inverse QTQt modeling (Gallagher, 2012) showing an eastward migrating phase of rapid bedrock cooling (vertical gray bar) from the (Aa) eastern Paria Peninsula, (b) western Northern Range, and (c) eastern Northern Range. The expected (weighted mean) thermal history is shown as a solid line and the 95% confidence intervals for the cold (highest elevation) and warm (lowest elevation) samples are shown with dashed lines. The red box shows the prior time-temperature model space. Thermal history constraints for $^{40}Ar/^{39}Ar$ data (Speed et al., 1997) in Paria and the western Northern Range are shown as a black box. QTQt model input data and additional model results are detailed in Table S7 and Figure S3. (d) Map of thermochronology samples (details in Table 1), highlighting the three structural-metamorphic regions and samples modeled (dashed circles and black sample symbols). The western and eastern Northern Range are defined in part by the occurrence of unreset and partially zircon fission track ages (white symbols; Algar et al., 1998; Weber, Ferrill, & Roden-Tice, 2001) dominantly in the eastern Northern range.

Factors that can cause single grain AHe ages that are anomalously older include internal crystal zonation, helium implantation from neighboring minerals, undetected inclusions (such as zircon) with high U and Th content, and alpha damage to the crystal lattice, which can trap helium (Flowers, 2009; Guenthner et al., 2013; Reiners & Farley, 2001). Conversely, the accumulation of significant radiation damage can cause helium traps to interconnect and increase helium diffusivity, which results in younger ages (Ault et al., 2019; Flowers, 2009). Radiation damage is likely the case for three single grain ages from samples T68 and T165 that have relatively high eU (186–794 ppm). Age dispersion in apatite grains due to radiation damage can also be caused by long residence at temperatures below the PRZ and reheating within the PRZ, which we also suspect influenced our ZHe data (Ault et al., 2019; Flowers, 2009; Guenthner et al., 2013; Reiners & Farley, 2001). These three aliquots did not fit intrasample eU versus age trends and were excluded from the thermal models. After removing four outlier grains, the range of single grain AHe ages from the Northern Range is 1.3 ± 1.0 to 6.0 ± 0.4 Ma and mean of all AHe ages is 4.0 ± 1.9 Ma (Tables 1 and S1 and Figures 3 and 4).

4.4. Spatial Pattern of Thermochronology Ages

Combined with published ages from the Northern Range and Paria Peninsula (Algar et al., 1998; Cruz et al., 2007; Weber, Ferrill, & Roden-Tice, 2001), the thermochronology ages generally young to the west (Figure 3). Along north-south transects, the youngest ages in the Paria Peninsula are located on the north (windward) side of the peninsula and adjacent to the North Coast fault zone offshore Trinidad (Figure 4; Cruz et al., 2007; Robertson & Burke, 1989). In the Northern Range, the youngest ages are located on the south (leeward) side of mountains and adjacent to the southern range-bounding Arima fault. The Northern Range is an exhumed fault block between the now inactive (normal?) Arima fault and active dextral-normal North Coast fault zones (Algar & Pindell, 1993; Weber, Ferrill, & Roden-Tice, 2001). Younger ages along the exhumed footwall block of the mountain flanks suggest that range-bounding faults may have helped facilitate rock uplift and exhumation. Old ages were found at high elevations in the eastern (ZHe: T68) and western (AFT: RCS916) Northern Range, which indicates elevation may be a possible control on cooling ages. However, most samples were collected between sea level and ~100 m and age-elevation relationships are not explored in detail here.

5. Thermal Modeling and Exhumation History

The QTQt expected models for the three regions are presented in Figure 5 and the model data and supporting results are in Figure S3 and Table S7. We convert average cooling rates from the expected models to calculate exhumation rates, assuming a constant paleo-geothermal gradient of 25°C/km and no isotherm advection due to exhumation or topography. The magnitude of exhumation is calculated from the exhumation rates and the highest temperature reset thermochronometer, which corresponds to ~20 Ma in each of the three regions. Because these assumptions may result in significant uncertainty (e.g., Mancktelow & Grasemann, 1997), we consider our exhumation calculations to be first-order estimates, that are used for comparison of the variation across the study area.

5.1. Paria Peninsula and Western Northern Range

The cooling histories of the Paria Peninsula and western Northern Range are similar to each other and show two substantial changes in cooling rate since the late Miocene (Figures 5 and S3). The QTQt models for these regions resulted in expected thermal histories that explain the data, which suggests that samples within these respective structural-metamorphic regions (Paria and western Northern Range) had a similar thermal history and that the joint inversion modeling approach is geologically reasonable.

The Paria and western Northern Range models exhibit poorly constrained *t-T* histories from ~30 Ma to ~15–9 Ma (Figures 5 and S3). This is likely due to a lack of zircon track and single-grain data from the western Northern Range and a large spread of ZFT and AFT ages from Paria. The thermal models indicate no, or very slow (<1°C/m.y.), bedrock cooling in these regions from ~30 Ma to ~15–9 Ma. Although model constraints during this time are wide, slow mid-Miocene cooling is supported by $^{40}Ar/^{39}Ar$ and ZFT ages from those regions. A simple linear cooling path extrapolated from the closure temperatures and ages of these higher-temperature thermochrometers to the expected thermal history at ~15–9 Ma, yields slow rates of cooling up to ~3°C/m.y.

The thermal histories show the time-averaged onset of rapid cooling is ~13 Ma (range is ~15–11 Ma; Figure S3) in the Paria Peninsula and is ~9 Ma (range is ~10–8 Ma: Figure S3) in the western Northern Range, at rates >30°C/m.y. The phase of rapid cooling was followed by a deceleration of cooling to <7°C/m.y. at ~7 Ma in the Paria Peninsula and at ~5 Ma in the western Northern Range (Figures 5 and S3).

The highest-temperature thermochronometer ($^{40}Ar/^{39}Ar$; Foland et al., 1992; Speed et al., 1997) indicates a total magnitude of rock exhumation to at least ~9 km since metamorphism at ~30–25 Ma in Paria and the western Northern Range. Notably, the majority of rock (~7 km) exhumed from these western regions occurred after the cessation of oblique plate collision at ~10 Ma. Exhumation rates during the early mid Miocene may have been negligible or up to ~0.3–0.1 mm/yr and then increased at ~13–9 Ma–~1.5–1.0 mm/yr in the west (Figure 5). Exhumation rates in the west decreased in the Pliocene to <0.4 mm/yr.

5.2. Eastern Northern Range

Initial modeling results from the eastern Northern Range failed to produce a credible expected model that incorporated all data from that region. This indicates the possibility of complex thermal histories from a lack of data, variations in localized tectonics, and/or that lateral spatial or structural position may control thermal histories in the eastern Northern Range (Gallagher, 2012). Considering the similarity of each thermochronology age system and equivalent metamorphic grade of rock exposed at similar structural levels in this region, we speculate that the lack of data from the eastern region is a source of model complexity (e.g., only two AFT samples have sufficient grains for modeling). This is supported by single sample models that produce similar patterns of cooling yet fail to produce credible models.

Two thermal models from the eastern Northern Range produced credible expected models and are presented in Figures 5 and S3 (Models C1, central and C2, north coast). The north coast thermal history predicts both AFT age and MTL within error, while both the north coast and central models yield well-predicted AHe ages and poorly predicted ZHe ages (Figure S3). Thermal histories from these eastern Northern Range sub-regions indicate negligible bedrock cooling, to cooling at a maximum of ~2°C/m.y. after metamorphism (Figure 5c). Cooling rates then increased at ~4 Ma (range of Models C1 and C2 is ~7–3 Ma) to ~20–15°C/m.y. (Figure S3). Unreset ZFT ages constrain the total magnitude of exhumation of the eastern Northern Range to ~6–4 km. Rapid exhumation initiated at approximately the beginning of the Pliocene at rates of ~1.5–0.5 mm/yr (Figure 5). There may be differences in localized cooling and exhumation within this region not captured in these models. We speculate that these differences are likely minor and assume that these sub-regions are generally representative of the eastern Northern Range.

6. Discussion

Combined with other data from the region (Algar et al., 1998; Cruz et al., 2007; Weber, Ferrill, & Roden-Tice, 2001) our thermal modeling indicates three phases of cooling and inferred exhumation from the Miocene to present in the eastern Paria Peninsula and Northern Range (Figure 5). Rapid cooling and inferred exhumation was followed by a deceleration of cooling, which appears to migrate with time eastward from the Paria Peninsula (~7 Ma) to the western Northern Range (~5 Ma). Nearly synchronous with the deceleration in the west, the onset of relatively fast cooling of the eastern Northern Range occurred (~4 Ma). Exhumation histories are reviewed in terms of these three phases and then possible mechanisms for driving exhumation of this coastal metamorphic mountain belt are explored.

6.1. Phase 1: Miocene Oblique Plate Collision

The first phase of cooling started after peak metamorphism at ~30–25 Ma (Foland et al., 1992; Speed et al., 1997) and lasted until ~13–9 Ma in eastern Paria and the western Northern Range (Figure 5). This period is characterized by the arrival of the south-southeast migrating Caribbean plate and oblique arc-continent collision in the Oligocene to dominantly the mid-Miocene in the study region (Figure 6; Babb & Mann, 1999; Pindell et al., 1998; Russo & Speed, 1992). In the foreland, oblique convergence uplifted and deformed the Late Cretaceous to early Neogene passive-sequence into a southward-vergent fold and thrust belt in eastern Venezuela and Trinidad (Figure 1; Erlich et al., 1993; Escalona & Mann, 2011; Giorgis et al., 2017). Interestingly, cooling rates (<3°C/m.y.) and exhumation (<0.2 mm/yr) in the western study area are relatively slow during this inferred period of plate convergence. Slow cooling and exhumation may be due to the distal location from the deformation front and the position of Paria and Northern Range sediments on the continental slope somewhat protected from erosion offshore. Although cooling was slow during this period, ~2–3 km of rock was exhumed in the western study area. The onset of exhumation coincides with the deposition of the Oligocene-Early Pliocene Cunapo Formation, which is a heterogeneous conglomerate deposited in the Northern Basin that fines and thins southward (Figure 2; Payne, 1991). Our new thermochronology data provide tighter constraints on both the timing and magnitude of syn-collisional exhumation and indicate relatively slow cooling and exhumation of Paria and the Northern Range.

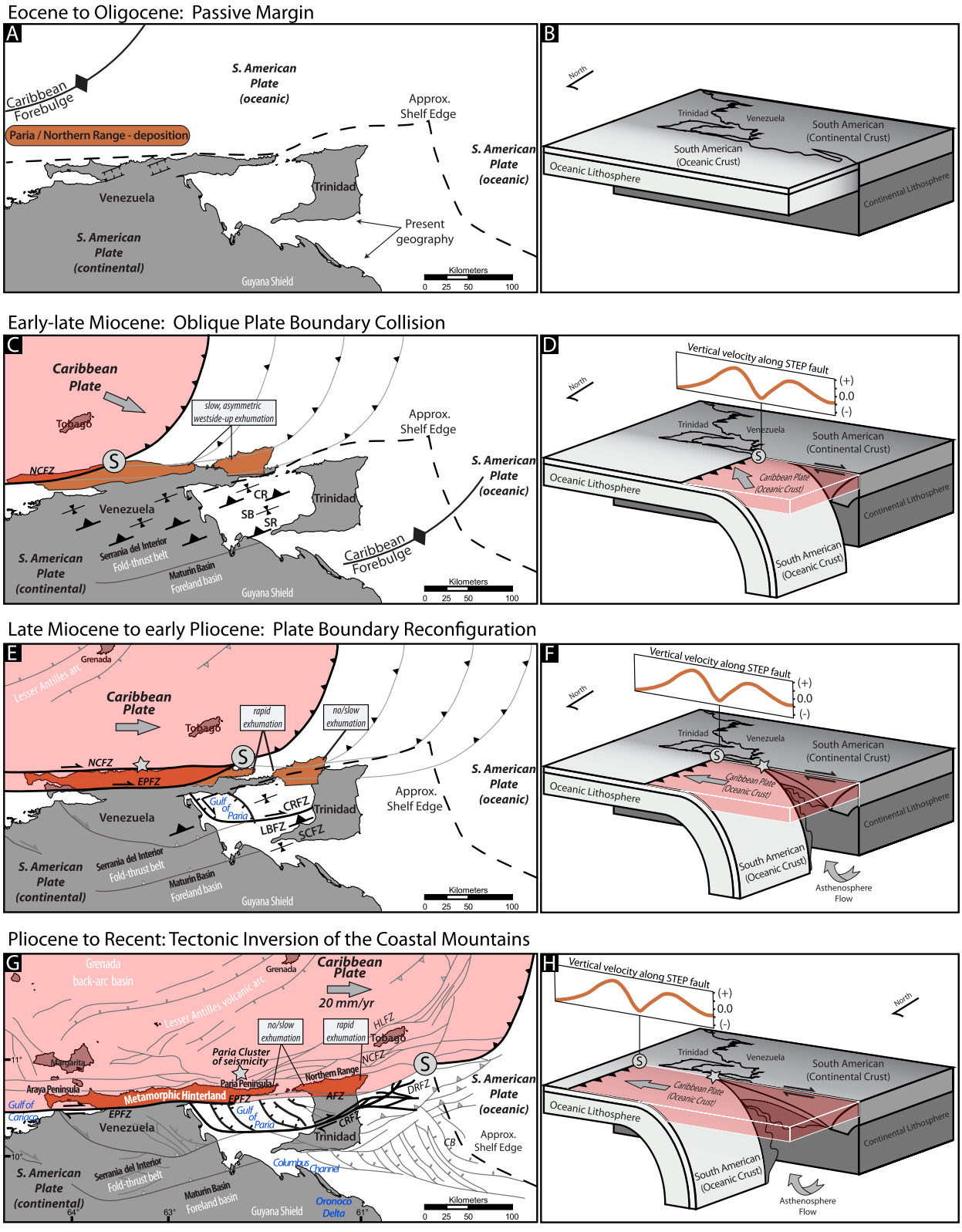
Eocene to Oligocene: Passive Margin
A
Caribbean Forebulge
S. American Plate (oceanic)
Approx. Shelf Edge
Paria / Northern Range - deposition
S. American Plate (oceanic)
Trinidad
Venezuela
Present geography
S. American Plate (continental)
Guyana Shield
Kilometers
0 25 50 100
B
North
Trinidad
Venezuela
South American (Continental Crust)
South American (Oceanic Crust)
Oceanic Lithosphere
Continental Lithosphere
Early-late Miocene: Oblique Plate Boundary Collision
C
Caribbean Plate
Tobago
slow, asymmetric westside-up exhumation
NCFZ
S
Approx. Shelf Edge
S. American Plate (oceanic)
CR
SB
SR
Trinidad
Venezuela
Caribbean Forebulge
S. American Plate (continental)
Serrania del Interior Fold-thrust belt
Maturin Basin Foreland basin
Guyana Shield
Kilometers
0 25 50 100
D
Vertical velocity along STEP fault
(+)
0.0
(-)
North
Trinidad
Venezuela
South American (Continental Crust)
Caribbean Plate (Oceanic Crust)
Oceanic Lithosphere
Continental Lithosphere
South American (Oceanic Crust)
Late Miocene to early Pliocene: Plate Boundary Reconfiguration
E
Grenada
Lesser Antilles arc
Caribbean Plate
Tobago
rapid exhumation
no/slow exhumation
NCFZ
EPFZ
S
Gulf of Paria
CRFZ
LBFZ
SCFZ
Trinidad
Venezuela
Approx. Shelf Edge
S. American Plate (oceanic)
S. American Plate (continental)
Serrania del Interior Fold-thrust belt
Maturin Basin Foreland basin
Guyana Shield
Kilometers
0 25 50 100
F
Vertical velocity along STEP fault
(+)
0.0
(-)
North
Trinidad
Venezuela
South American (Continental Crust)
Caribbean Plate (Oceanic Crust)
Oceanic Lithosphere
Continental Lithosphere
South American (Oceanic Crust)
Asthenosphere Flow
Pliocene to Recent: Tectonic Inversion of the Coastal Mountains
G
Grenada
back-arc basin
Grenada
Caribbean Plate
20 mm/yr
Lesser Antilles volcanic arc
no/slow exhumation
rapid exhumation
HLFZ
Tobago
Paria Cluster of seismicity
NCFZ
S
Margarita
Araya Peninsula
Paria Peninsula
Northern Range
DRFZ
Metamorphic Hinterland
EPFZ
AFZ
S. American Plate (oceanic)
Gulf of Cariaco
Gulf of Paria
CRFZ
Venezuela
Trinidad
CB
Approx. Shelf Edge
Columbus Channel
S. American Plate (continental)
Serrania del Interior Fold-thrust belt
Maturin Basin Foreland basin
Guyana Shield
Orinoco Delta
Kilometers
0 25 50 100
H
Vertical velocity along STEP fault
(+)
0.0
(-)
North
Trinidad
Venezuela
South American (Continental Crust)
Caribbean Plate (Oceanic Crust)
Oceanic Lithosphere
Continental Lithosphere
South American (Oceanic Crust)
Asthenosphere Flow

Figure 6.

6.2. Phase 2: Late Miocene to Early Pliocene Plate Boundary Reconfiguration

The second phase of deformation is marked by an abrupt ~six-fold increase in cooling and exhumation starting at ~13–9 Ma in Paria and the western Northern Range and lasted until the latest Miocene to Pliocene (Figures 5a and 5b). The amount of exhumation was likely insufficient to expose rocks that were hotter than ~120°C in the east at the onset of the event. This time is characterized by a presumed change from oblique plate convergence to transform motion ~10 Ma, and extension and sediment accumulation in the Gulf of Paria (Babb & Mann, 1999; Escalona & Mann, 2011; Flinch et al., 1999; Pindell et al., 1998). A thick stratal succession of Cunapo conglomerate to the south of the Northern Range marks a mid-Miocene angular unconformity, which is interpreted to represent the onset of significant erosion of the Northern Range (Payne, 1991; Pindell et al., 1998).

Strike-slip motion during this time was accommodated on the El Pilar fault south of the Paria Peninsula and began to shift southward to the Central Range, Los Bajos, and Soldado (South Coast) fault zones in Trinidad (Figure 2) (Babb & Mann, 1999). To the south of the Paria Peninsula, half-grabens developed along steeply dipping normal faults and accommodated a large influx of late Miocene to Pliocene sediments in the Gulf of Paria pull-apart basin (Flinch et al., 1999). The rapid rates (~1.5 mm/yr) and large magnitude (~7 km) of rock exhumed in the Paria Peninsula and the western Northern Range are consistent with extension and the large sediment influx into the peripheral basins. However, it is notable that during this phase characterized by strike-slip motion, exhumation rates and the total amount of exhumation in the western study area were substantially greater than during the previous phase of presumed mid-Miocene convergence.

6.3. Phase 3: Pliocene to Recent Tectonic Inversion of the Coastal Mountains

The third phase of cooling is characterized by an inversion in the locus of rapid bedrock exhumation rates from the western to the eastern Northern Range in the Pliocene (Figures 3 and 5). Rapid exhumation in the western study area decelerated to <0.4 mm/yr at ~7 Ma in the Paria Peninsula and perhaps slightly later, and ~5 Ma, in the western Northern Range. As bedrock exhumation in the western study area was decreasing, cooling and exhumation in the eastern Northern Range increased to ~1.0 mm/yr (Figure 5). Regionally, the magnitude of exhumation of the coastal metamorphic mountains is limited to only ~1–2 km since the Pliocene. This low magnitude of exhumation predicts waning sedimentation rates into the Gulf of Paria and in the Northern Basin (Babb & Mann, 1999; Flinch et al., 1999; Payne, 1991). Extension and subsidence of the Gulf of Paria pull-apart basin occurred in the middle Pliocene to Pleistocene as the Central Range fault became the principal strike-slip fault in Trinidad (e.g., Flinch et al., 1999; Babb & Mann, 1999). In response to subsidence in the Gulf of Paria, the east-side-up tilting observed in the western Northern Range is generally constrained to the Pliocene and Quaternary (Figure 3; Arkle, Owen, Weber, Caffee, & Hammer, 2017; Ritter & Weber, 2007; Weber, 2005). The synchronous change in exhumation rates defined by the AHe ages more narrowly constrains the inversion to east-side-up tilting of the Northern Range to have occurred at ~4 Ma.

Figure 6. Tectonic evolution of the southeast Caribbean (modified after Algar & Pindell, 1993; Bezada et al., 2010; Miller et al., 2009). Inset graph shows the vertical velocity of crustal and topographic changes (orange line) relative to subduction-transform edge propagator (STEP) fault propagation (from Govers & Wortel, 2005). The geography and Paria cluster of seismicity (gray star) along the STEP fault zone (Russo & Speed, 1992) and location of the STEP (Nijholt & Govers, 2015; gray circle with "S") are inferred based on modern plate rates (Weber, Dixon, et al., 2001; Weber et al., 2011). (a–b) Deposition of the Paria and Northern Range rocks on a Jurassic-Cretaceous north-facing passive margin (Algar & Pindell, 1993; Pindell et al., 1998). (c–d) Flexural forebulge passes continental South America and south-southeast migration of the Caribbean plate causes asymmetric exhumation and uplift of the passive margin sediments forming the coastal metamorphic hinterland. (e–f) Caribbean-South American plate boundary steps inboard and changes to east-directed transform motion. The arrival of the STEP edge within the vicinity of Paria and Northern Range. Rapid exhumation of Paria and the western Northern Range initiates either by STEP flexure and/or transtension. (g–h) The Central Range fault becomes the principal strike-slip fault in Trinidad and enhances extension and subsidence of the Gulf of Paria pull-apart (Babb & Mann, 1999). As the STEP edge passes, upward crustal flexure propagates eastward under the eastern Northern Range and in the wake of the STEP, subsidence may also be enhanced and/or caused by downward flexure associated with lithospheric tearing along the STEP fault (EPFZ) in the Gulf of Paria region. EPFZ–El Pilar fault zone; AFZ–Arima fault zone; CRFZ–Central Range fault zone; DRFZ–Darien Ridge fault zone; CB–Columbus Basin; NCFZ–North Coast fault zone; HLFZ–Hinge Line fault zone; LBFZ–Los Bajos fault zone; SCFZ–South Coast fault zone; CR–Central Range.

6.4. Implications for the Tectonic Evolution of the Southeast Caribbean

Our new thermochronology data support that oblique Caribbean-South American collision may have occurred generally during the Miocene in Trinidad and eastern Venezuela (Figures 5 and 6). However, we observed a pattern of westward decreasing thermochronology ages from the region and exhumation that post-dates the presumed oblique collision (Figures 3 and 5). These new observations are in opposition to those qualitatively predicted by an eastward migrating and colliding Caribbean plate. In addition, our data reveal inconsistencies between our observed substantial increase in exhumation, which occurred nearly synchronously with the presumed change to transform plate motion ~10 Ma, and the observation that these rapid rates of exhumation were then sustained for ~5–7 m.y. until the Pliocene (Figure 5). We review potential mechanisms that could have driven post-collision exhumation, which include isostatic rebound of a thickened crustal root, erosional unloading, exhumation along tectonic restraining and releasing bends, and/or lithospheric detachment process associated with STEP fault deformation.

Algar et al. (1998) hypothesized that isostatic rebound of the Northern Range might have resulted in continued exhumation during gravitational collapse of a shortened and thickened crust that developed during Miocene oblique convergence. Cruz et al. (2007) infer that erosion enhanced an isostatic response of a buoyant crustal root, which they suggest to be thickest closest to the Caribbean indenter. Numerical models show that surface erosion can cause exhumation of crustal roots for hundreds of millions of years after active tectonism has ceased and at rates greater than during collision (Fischer, 2002). With the progressive loss of surface mass and buoyancy of the crustal root, however, the magnitude and rates of exhumation should both be significantly reduced over time (Fischer, 2002; Koyi et al., 1999). An overthickened crust could lead to the buoyant rise of the metamorphic coastal mountain belt, yet an isostatic response of a buoyant crustal root would require these mountains to overcome the flexural rigidity of the lithosphere (Turcotte & Schubert, 2014). Flexural rigidity along the thinned northern margin of continental South America is lower than that of the continental interior to the south (Miller et al., 2009; Pindell et al., 1998). However, the ~15-km-wide mountain range is likely far too narrow to have achieved isostatic equilibrium (e.g., Turcotte & Schubert, 2014). If isostatic equilibrium was achieved, it is questionable whether gravitational collapse and exhumation related to isostasy would occur at greater rates than those during crustal shortening and thickening such as the six-fold mid-Miocene increase we document here.

An additional driver, such as focused erosion, delamination or detachment of lithosphere, or plate flexure could enhance uplift and exhumation of an over-thickened crust (e.g., Molnar et al., 1993). Erosional unloading above a thickened root seems unlikely given that the westward decreases in modern precipitation rates are in opposition to this effect, and given the low rates of surface erosion measured in these mountains (Arkle, Owen, Weber, Caffee, & Hammer, 2017). Slab break-off processes, associated with the South American passive margin that was subducted during oblique convergence (e.g., Speed, 1985), could cause a rapid buoyant rise of the coastal mountains. However, a descending lithospheric slab, which would counteract the positive buoyancy of a crustal root, would have had to detach nearly coincident with the cessation of oblique collision to have generated the abrupt observed increase of exhumation at ~13–9 Ma. Moreover, new high-resolution seismic tomography indicates that continental South American lithosphere is still currently attached to the subducting oceanic South American lithosphere east of the Paria cluster of seismicity, that is, in our study area (Figure 2; Bezada et al., 2010; VanDecar et al., 2003; Miller et al., 2009; Levander et al., 2014). Thus, we find it problematic to attribute our observed mid-Miocene increase in exhumation exclusively to the buoyant rise of a crustal root. Without a detached slab under the study area, it seems unlikely that the buoyant rise of a thickened crustal root could overcome the viscous drag or slab pull of a subducting slab. Given the above considerations, the thermochronology data we present here do not support, but also do not quantitatively exclude an isostatic response of a buoyant crustal root as the principal mechanism driving exhumation.

We consider the possibility that the rapid exhumation revealed here may be caused or enhanced by a propagating STEP that has advanced eastward under the coastal mountain ranges we studied (Figure 6). Geodynamic modeling indicates that motions focused at the edge of a STEP fault can cause kilometer-scale downward flexure of the lithosphere and topographic subsidence along the transform plate boundary (Figure 6 inset graphs; Govers & Wortel, 2005). In front of the STEP, lateral lithospheric resistance to tear propagation can cause upward flexural bulging of the lithosphere and surface uplift before tearing, over horizontal

distances of a couple of hundreds of kilometers (Clark, Sobiesiak, et al., 2008; Govers & Wortel, 2005). This could produce exhumation and uplift around the STEP that is then followed by subsidence as the STEP moves through the landscape (Figure 6; Govers & Wortel, 2005; Wortel et al., 2009).

The presence of a STEP fault in the location needed to explain our observations, that is, currently under Trinidad and Venezuela's coastal metamorphic mountains, is consistent with geophysical observations. Broadband seismic data (Clark, Zelt, et al., 2008; Levander et al., 2014) and surface wave tomography (Miller et al., 2009) show that the continental lithosphere south and west of the Paria cluster and the El Pilar fault is thin and dips northward toward the plate boundary (Miller et al., 2009). Downward flexure of the lithosphere is also consistent with the observed extremely negative Bouguer and free air gravity anomalies in the region (Russo and Speed, 1992, Russo et al., 1993). These data indicate that the surface topography of the Paria coastal range is ~3 km lower than expected from Airy gravity compensation (Russo & Speed, 1992). The site of the proposed active STEP fault zone (El Pliar fault zone) coincides with the lowest-present-day elevations of the coastal mountains, and is focused near the Gulf of Paria; topography systematically increases both to the west and to the east of the Gulf of Paria (Figures 1 and 2). Crustal flexure between the STEP fault zone and the STEP (located northeast of Trinidad) may enhance or cause the observed transition from active uplift of the eastern Northern Range to active subsidence of the western Northern Range and eastern Paria (Figures 6h and 3; Arkle, Owen, Weber, Caffee, & Hammer, 2017). This region of topographic subsidence around the Gulf of Paria currently spans ~100 km in diameter, but also coincides with shallow normal faulting related to the right-step of the active plate boundary.

Our data indicate an ~six-fold increase in cooling and exhumation ~13–9 Ma, which occurred after oblique collision. During this time the eastern Paria Peninsula and western Northern Range would have been in front of the STEP at the onset of this phase of rapid exhumation (Figure 6e). Assuming current plate motion rates (~20 mm/yr), we infer that flexural bulging associated with the STEP could have reached this area ~100–200 km in front of the STEP (Figure 6f). This could have resulted in or enhanced gravitational collapse of a thickened buoyant crust post-collision. Long-term crustal extension is apparent from kinematic fault data from southern Tobago, which indicates N-S stretching on E-W striking normal faults from the Pliocene to Pleistocene (Ringerwole et al., 2011). In addition, our thermal models show that the onset of rapid exhumation initiated first in Paria at ~13 Ma and then in the western Northern Range at ~9 Ma. Given the overlap of the timing obtained, more data could perhaps help constrain this apparent migration. During the mid-Miocene, the eastern Northern Range would have been located ~200–300 km in front of the STEP, and apparently on the leading front of deformation associated with flexural bulging, resulting in relatively little exhumation that we document there.

The arrival of the STEP edge to within <100 km of the eastern Paria Peninsula and western Northern Range would have occurred roughly in the late Pliocene. We infer that the lithosphere under Paria and the western Northern Range by this time could have been flexed downward, while a flexural bulge had propagated to the eastern Northern Range. This timing coincides with the deceleration of exhumation, first in the Paria Peninsula at ~7 Ma and then in western Northern Range at ~5 Ma. Synchronously, at ~4 Ma, exhumation accelerated in the eastern Northern Range. Recent earthquake activity along the sub-Tobago terrane boundary and coeval northward sliding on a low angle (28°) north-dipping normal fault between Trinidad and Tobago indicates reactivation and inversion of the CA-SA suture zone (Weber et al., 2015). The development of normal faults and extension of the upper crust as a result of flexural bulging is consistent with shallow stress-fields modeled for STEP faulting (Govers & Wortel, 2005) and is observed in other known tear fault localities (e.g., Gallais et al., 2013; Polonia et al., 2016). The overall slow rates and shallow magnitudes of exhumation post-Pliocene we observe are consistent with low rates of surface erosion measured over millennial-timescales (Arkle, Owen, Weber, Caffee, & Hammer, 2017), and enhanced subsidence in the Gulf of Paria pull-apart basin (Babb & Mann, 1999; Flinch et al., 1999).

Whether or not lithospheric flexure related to deep STEP faulting has and is influencing exhumation and uplift along the plate boundary, our thermochronology data require a significant amount of total exhumation (>7 km) since oblique collision in the mid-Miocene. This magnitude of vertical crustal motion across the mountains is within range of numerical modeled STEP fault amplitudes (Govers & Wortel, 2005). We suggest that this exhumation was driven by slip along the North Coast Fault zone and additional structures north of the mountains (e.g., Algar & Pindell, 1993; Babb & Mann, 1999; Flinch et al., 1999). If exhumation

in the study region is related to STEP kinematics, our data indicate that STEP faults and associated processes are capable of exhuming rock on the order of several kilometers, or perhaps even more depending on local boundary conditions. The migration of deformation and exhumation over discrete time periods and spatial scales presents new insights for geodynamic models and our study provides some of the first empirical datasets that may document the long-term (10^6 years) deformation patterns associated with STEP plate corners. If the STEP model proves to be correct, the established oblique collision to transform plate motion model for the Caribbean-South American boundary would have to be reconsidered in light of plate flexure migrating eastward as a contractile wave followed by transform deformation.

7. Conclusions

Thermochronometry data (AHe, AFT, and ZHe) and thermal history modeling from the eastern Paria Peninsula and Northern Range constrain three tectonic phases. The first phase is related to oblique Caribbean-South American plate convergence and is characterized by relatively slow cooling and inferred exhumation rates of <0.2 mm/yr that started after peak metamorphism at ~30–25 Ma and lasted until ~13–9 Ma. The subsequent change from oblique plate convergence to transform motion was characterized by extension and sediment accumulation in the Gulf of Paria. Near the onset of change in plate boundary configuration, there was an increase in exhumation rates up to ~1.5 mm/yr starting at ~13 Ma in the Paria Peninsula and at ~9 Ma western Northern Range. These high rates of exhumation lasted roughly until the late Miocene-early Pliocene. The last tectonic phase is defined by an inversion in the exhumation pattern, which occurred throughout the Pliocene. While exhumation rates decelerated to <0.4 mm/yr starting at ~7 Ma in the Paria Peninsula and at ~5 Ma in the western Northern Range, exhumation of the eastern Northern Range increased to ~1.0 mm/yr at ~4 Ma. We interpret that this temporal and spatial pattern of rock exhumation along the Caribbean-South American plate boundary is consistent with the time-transgressive deformation produced by an eastward propagating lithospheric STEP fault and associated processes of dynamic mantel flow and crustal extension. Geodynamic STEP processes may have driven crustal extension and collapse of the buoyant, overthickened crust and/or enhanced these relatively shallow crustal processes in this region.

Data Availability Statement

The thermochronology data sets presented here are provided in the Supporting Information and are published in the Geochron Library: AHe data: https://www.geochron.org/viewfile.php?pkey=16601; ZHe data: https://www.geochron.org/viewfile.php?pkey=16602; AFT data: https://www.geochron.org/viewfile.php?pkey=16603.

Acknowledgments
We thank Philip Farfan, Xavier Moonan, Vishal Nagassar, Roger Kimber, and Nigel Noriega for geologic discussions and logistical support in the field. Sarah Hammer is thanked for assistance with sample preparation at the University of Cincinnati. We thank Becky Flowers, Jim Metcalf, and the staff at the TRaIL lab, University of Boulder, for performing (U-Th)/He measurements. This contribution is part of JCA's dissertation research at the University of Cincinnati. We are grateful to our funders for this project, which was provided by the University Research Council of the University of Cincinnati as a Graduate Student Research Fellowship granted to L. A. Owen and J. C. Arkle and a research grant from Centrica Energy, Trinidad to J. C. Arkle and J. C. Weber. We thank Cheyenne Bartelt for assistance with figures. We appreciate the insightful and thorough reviews by Sebastian Zapata and Mauricio Parra that greatly improved this paper.

References

Algar, S., Heady, E. C., & Pindell, J. L. (1998). Fission-track dating in Trinidad: Implications for provenance, depositional timing and tectonic uplift. Paleogeographic Evolution and Non-Glacial Eustasy, northern South America, 58(1), 111–128. https://doi.org/10.2110/pec.98.58.0111

Algar, S., & Pindell, J. L. (1993). Structure and deformation history of the Northern Range of Trinidad and adjacent areas. *Tectonics*, *12*(4), 814–829. https://doi.org/10.1029/93tc00673

Alvarez, T. G. (2014). The southeastern Caribbean subduction to strike-slip transition zone: A study of the effects on lithospheric structures and overlying clastic basin evolution and fill [Ph. D. Dissertation] (p. 257). The University of Texas at Austin.

Arkle, J. C., Armstrong, P. A., Haeussler, P. J., Prior, M. G., Hartman, S., Sendziak, K. L., & Brush, J. A. (2013). Mechanisms of rock uplift above flat slab subduction in the western Chugach Mountains and Prince William Sound of the southern Alaska syntaxis. *Geological Society of America Bulletin*, *125*, 776–793. https://doi.org/10.1130/b30738.1., v.

Arkle, J. C., Owen, L. A., & Weber, J. C. (2017). Trinidad and Tobago. In C. D. Allen (Ed.), *Landscapes and landforms of the lesser Antilles* (pp. 267–291). Cham. Springer International Publishing. https://doi.org/10.1007/978-3-319-55787-8_17

Arkle, J. C., Owen, L. A., Weber, J. C., Caffee, M. W., & Hammer, S. (2017). Transient Quaternary erosion and tectonic inversion of the Northern Range, Trinidad. *Geomorphology*, *295*, 337–353. https://doi.org/10.1016/j.geomorph.2017.07.013

Ault, A. K., Gautheron, C., & King, G. E. (2019). Innovations in (U–Th)/He, fission track, and trapped charge thermochronometry with applications to earthquakes, weathering, surface-mantle connections, and the growth and decay of mountains. *Tectonics*, *38*(11), 3705–3739. https://doi.org/10.1029/2018TC005312

Babb, S., & Mann, P. (1999). Structural and sedimentary development of a Neogene transpressional plate boundary between the Caribbean and South America plates in Trinidad and the Gulf of Paria. In P. Mann (Ed.), Sedimentary basins of the world (Vol. 4, pp. 495–557). Elsevier. https://doi.org/10.1016/s1874-5997(99)80052-5

Baes, M., Govers, R., & Wortel, R. (2011). Subduction initiation along the inherited weakness zone at the edge of a slab: Insights from numerical models. *Geophysical Journal International*, *184*(3), 991–1008. https://doi.org/10.1111/j.1365-246x.2010.04896.x

Bezada, M. J., Levander, A., & Schmandt, B. (2010). Subduction in the southern Caribbean: Images from finite-frequency P wave tomography. *Journal of Geophysical Research*, *115*(12), B12333. https://doi.org/10.1029/2010jb007682

Bilich, A., Frohlich, C., & Mann, P. (2001). Global seismicity characteristics of subduction-to-strike-slip transitions. *Journal of Geophysical Research*, *106*(B9), 19443–19452. https://doi.org/10.1029/2000jb900309

Brandon, M. T., Roden-Tice, M. K., & Garver, J. I. (1998). Late Cenozoic exhumation of the Cascadia accretionary wedge in the Olympic Mountains, northwest Washington State. *Geological Society of America Bulletin*, *110*, 985–1009. https://doi.org/10.1130/0016-7606(1998)110<0985:lceotc>2.3.co;2

Clark, S. A., Levander, A., Magnani, M. B., & Zelt, C. A. (2008). Negligible convergence and lithospheric tearing along the Caribbean–South American plate boundary at 64°W. *Tectonics*, *27*(6), TC6013. https://doi.org/10.1029/2008tc002328

Clark, S. A., Sobiesiak, M., Zelt, C. A., Magnani, M. B., Miller, M. S., Bezada, M. J., & Levander, A. (2008). Identification and tectonic implications of a tear in the South American plate at the southern end of the Lesser Antilles. *Geochemistry, Geophysics, Geosystems*, *9*(11), Q11004. https://doi.org/10.1029/2008gc002084

Clark, S. A., Zelt, C. A., Magnani, M. B., & Levander, A. (2008). Characterizing the Caribbean–South American plate boundary at 64°W using wide-angle seismic data. *Journal of Geophysical Research*, *113*, B07401. https://doi.org/10.1029/2007jb005329

Cruz, L., Fayon, A., Teyssier, C., & Weber, J. (2007). Exhumation and deformation processes in transpressional orogens: The Venezuelan Paria Peninsula, SE Caribbean-South American plate boundary. In A. B. Till, S. M. Roeske, J. C. Sample, & D. A. Foster (Eds.), Exhumation associated with continental strike-slip systems (Vol. 434, pp. 149–165). Geological Society of America Special Paper. https://doi.org/10.1130/2007.2434(08)

de Verteuil, L., Ramlal, B., & Weber, J. (2006). *Trinidad geological GIS–module 1–surface geology and geography*. Port-of-Spain, Trinidad. Latinum Ltd.

Dodson, M. H. (1973). Closure temperature in cooling geochronological and petrolog-ical systems. *Contributions to Mineralogy and Petrology*, *40*, 259–274. https://doi.org/10.1007/bf00373790

Donelick, R. A., O'Sullivan, P. B., & Ketcham, R. A. (2005). Apatite fission-track analysis. *Reviews in Mineralogy and Geochemistry*, *58*, 49–94. https://doi.org/10.2138/rmg.2005.58.3

Enkelmann, E., Zeitler, P. K., Pavlis, T. L., Garver, J. I., & Ridgway, K. D. (2009). Intense localized rock uplift and erosion in the St Elias orogen of Alaska. *Nature Geoscience*, *2*(5), 360–363. https://doi.org/10.1038/ngeo502

Erlich, R. N., Farfan, P. F., & Hallock, P. (1993). Biostratigraphy, depositional environments, and diagenesis of the Tamana Formation, Trinidad: A tectonic marker horizon. *Sedimentology*, *40*(4), 743–768. https://doi.org/10.1111/j.1365-3091.1993.tb01358.x

Escalona, A., & Mann, P. (2011). Tectonics, basin subsidence mechanisms, and paleogeography of the Caribbean-South American plate boundary zone. *Marine and Petroleum Geology*, *28*(1), 8–39. https://doi.org/10.1016/j.marpetgeo.2010.01.016

Farley, K. A. (2000). Helium diffusion from apatite: General behavior as illustrated by Durango fluorapatite. *Journal of Geophysical Research*, *105*, 2903–2914. https://doi.org/10.1029/1999jb900348

Farley, K. A. (2002). (U-Th)/He dating: Techniques, calibrations, and applications. In D. Porcelli, C. J. Ballentine, & R. Wieler (Eds.), Noble gases in Geochemistry and Cosmochemistry: Reviews of mineralogy (Vol. 47, pp. 819–844). Mineralogical Society of America. https://doi.org/10.1515/9781501509056-020

Fischer, K. M. (2002). Waning buoyancy in the crustal roots of old mountains. *Nature*, *417*, 933–936. https://doi.org/10.1038/nature00855

Flinch, J. F., Rambaran, V., Ali, W., Lisa, V. D., Hernández, G., Rodrigues, K., & Sams, R. (1999). Structure of the Gulf of Paria pull-apart basin (Eastern Venezuela-Trinidad). In P. Mann (Ed.), Sedimentary basins of the world (Vol. 4, pp. 477–494). Elsevier. https://doi.org/10.1016/s1874-5997(99)80051-3

Flowers, R. M. (2009). Exploiting radiation damage control on apatite (U-Th)/He dates in cratonic regions. *Earth and Planetary Science Letters*, *277*(1–2), 148–155. https://doi.org/10.1016/j.epsl.2008.10.005

Flowers, R. M., Farley, K. A., & Ketcham, R. A. (2015). A reporting protocol for thermochronologic modeling illustrated with data from the Grand Canyon. *Earth and Planetary Science Letters*, *432*, 425–435. https://doi.org/10.1016/j.epsl.2015.09.053

Flowers, R. M., Ketcham, R. A., Shuster, D. L., & Farley, K. A. (2009). Apatite (U-Th)/He thermochronometry using a radiation damage accumulation and annealing model. *Geochimica et Cosmochimica Acta*, *73*, 2347–2365. https://doi.org/10.1016/j.gca.2009.01.015

Foland, K. A., Speed, R., & Weber, J. (1992). Geochronologic studies of the hinterland of the Caribbean orogen of Venezuela and Trinidad. *Geological Society of America Abstracts with Programs*, *24*(7), A148.

Forsyth, D. W. (1975). Fault plane solutions and tectonics of the South Atlantic and Scotia Sea. *Journal of Geophysical Research*, *80*(11), 1429–1443. https://doi.org/10.1029/jb080i011p01429

Frey, M., Saunders, J., & Schwander, H. (1988). The mineralogy and metamorphic geology of low-grade metasediments, Northern Range, Trinidad. *Journal of the Geological Society*, *145*(4), 563–575. https://doi.org/10.1144/gsjgs.145.4.0563

Fukuda, S., Sueoka, S., Kohn, B. P., & Tagami, T. (2020). (U–Th)/He thermochronometric mapping across the northeast Japan Arc: Towards understanding mountain building in an island - Arc setting. *Earth, Planets and Space*, *72*, 24. https://doi.org/10.1186/s40623-020-01151-z

Galbraith, R. F. (1990). The radial plot: Graphical assessment of spread in ages. *Nuclear Tracks and Radiation Measurements*, *17*(3), 207–214. https://doi.org/10.1016/1359-0189(90)90036-w

Gallagher, K. (2012). Transdimensional inverse thermal history modeling for quantitative thermochronology. *Journal of Geophysical Research*, *117*(B2), B02408. https://doi.org/10.1029/2011JB008825

Gallais, F., Graindorge, D., Gutscher, M. A., & Klaeschen, D. (2013). Propagation of a lithospheric tear fault (STEP) through the western boundary of the Calabrian accretionary wedge offshore eastern Sicily (southern Italy). *Tectonophysics*, *602*, 141–152. https://doi.org/10.1016/j.tecto.2012.12.026

Garciacaro, E., Mann, P., & Escalona, A. (2011). Regional structure and tectonic history of the obliquely colliding Columbus foreland basin, offshore Trinidad and Venezuela. *Marine and Petroleum Geology*, *28*(1), 126–148. https://doi.org/10.1016/j.marpetgeo.2009.08.016

Giorgis, S., Weber, J., Sanguinito, S., Beno, C., & Metcalf, J. (2017). Thermochronology constraints on Miocene exhumation in the Central Range Mountains, Trinidad. *Geological Society of America Bulletin*, *129*(1–2), 171–178. https://doi.org/10.1130/B31363.1

González de Juana, C., Muñoz, N., & Vignali, M. (1972). Reconocimiento Geológico de la Península de Paria, Venezuela: Memoria Cuarto Congreso Geológico Venezolano, Tomo III, p. 1549–1588.

Govers, R., & Wortel, M. J. R. (2005). Lithosphere tearing at STEP faults; response to edges of subduction zones. *Earth and Planetary Science Letters*, *236*, 505–523. https://doi.org/10.1016/j.epsl.2005.03.022

Green, P. F., Duddy, I. R., Gleadow, A. J. W., Tingate, P. R., & Laslett, G. M. (1986). Thermal annealing of fission-tracks in apatite: 1. A quantitative description. *Chemical Geology: Isotope Geoscience section*, *59*, 237–253. https://doi.org/10.1016/0168-9622(86)90074-6

Guenthner, W. R., Reiners, P. W., Ketcham, R. A., Nasdala, L., & Giester, G. (2013). Helium diffusion in natural zircon: Radiation damage, anisotropy, and the interpretation of zircon (U-Th)/He thermochronology. *American Journal of Science*, *313*(3), 145–198. https://doi.org/10.2475/03.2013.01

Hijmans, R. J., Cameron, S. E., Parra, J. L., Jones, P. G., & Jarvis, A. (2005). Very high resolution interpolated climate surfaces for global land areas. *International Journal of Climatology: A Journal of the Royal Meteorological Society*, *25*(15), 1965–1978. https://doi.org/10.1002/joc.1276

Ketcham, R. A., Carter, A. C., Donelick, R. A., Barbarand, J., & Hurford, A. J. (2007). Improved measurement of fission-track annealing in apatite using *c*-axis projection. *American Mineralogist*, *92*, 789–798. https://doi.org/10.2138/am.2007.2280

Koons, P. O., Hooks, B. P., Pavlis, T. L., Upton, P., & Barker, A. D. (2010). Three-dimensional mechanics of Yakutat convergence in the southernAlaskan plate corner. *Tectonics*, *29*, TC4008. https://doi.org/10.1029/2009TC002463

Koyi, H. A., Milnes, A. G., Schmeling, H., Talbot, C. J., Juhlin, C., & Zeyen, H. (1999). Numerical models of ductile rebound of crustal roots beneath mountain belts. *Geophysical Journal International*, *139*(2), 556–562. https://doi.org/10.1046/j.1365-246x.1999.00978.x

Levander, A., Bezada, M. J., Niu, F., Humphreys, E. D., Palomeras, I., Thurner, S. M., et al. (2014). Subduction-driven recycling of continental margin lithosphere. *Nature*, *515*(7526), 253–256. https://doi.org/10.1038/nature13878

Mancktelow, N. S., & Grasemann, B. (1997). Time-dependent effects of heat advection and topography on cooling histories during erosion. *Tectonophysics*, *270*(3–4), 167–195. https://doi.org/10.1016/s0040-1951(96)00279-x

Mann, P. (2007). Global catalogue, classification and tectonic origins of restraining-and releasing bends on active and ancient strike-slip fault systems. *Geological Society, London, Special Publications*, *290*(1), 13–142. https://doi.org/10.1144/sp290.2

McCaffrey, R., Qamar, A. I., King, R. W., Wells, R., Khazaradze, G., Williams, C. A., et al. (2007). Fault locking, block rotation, and crustal deformation in the Pacific Northwest. *Geophysical Journal International*, *169*, 1315–1340. https://doi.org/10.1111/j.1365-246X.2007.03371

Miller, M. S., Levander, A., Niu, F., & Li, A. (2009). Upper mantle structure beneath the Caribbean-South American plate boundary from surface wave tomography. *Journal of Geophysical Research*, *114*(B1), B01312. https://doi.org/10.1029/2007jb005507

Molnar, P., England, P., & Martinod, J. (1993). Mantle dynamics, uplift of the Tibetan Plateau, and the Indian monsoon. *Reviews of Geophysics*, *31*(4), 357–396. https://doi.org/10.1029/93rg02030

Molnar, P., & Sykes, L. R. (1969). Tectonics of the Caribbean and Middle America regions from focal mechanisms and seismicity. *Geological Society of America Bulletin*, *80*, 1639–1684. https://doi.org/10.1130/0016-7606(1969)80[1639:totcam]2.0.co;2

Nijholt, N., & Govers, R. (2015). The role of passive margins on the evolution of subduction-transform edge propagators (STEPs). *Journal of Geophysical Research: Solid Earth*, *120*(10), 7203–7230. https://doi.org/10.1002/2015jb012202

Özbakir, A. D., engör, A. M. C., Wortel, M. J. R., & Govers, R. (2013). The Pliny-Strabo trench region: A large shear zone resulting from slab tearing. *Earth and Planetary Science Letters*, *325*, 188–195.

Payne, N. (1991). An evaluation of post-Middle Miocene geological sequences, offshore Trinidad, Transactions of the 2nd Geological Conference of the Geological Society of Trinidad and Tobago, Port-of-Spain, Trinidad.

Pindell, J., Kennan, L., Maresch, W. V., Stanek, K., Draper, G., & Higgs, R. (2005). Plate-kinematics and crustal dynamics of circum-Caribbean arc-continent interactions: Tectonic controls on basin development in Proto-Caribbean margins. *Special Papers - Geological Society of America*, *394*, 7. https://doi.org/10.1130/0-8137-2394-9.7

Pindell, J. L., Higgs, R., & Dewey, J. F. (1998). Cenozoic palinspastic reconstruction, paleogeographic evolution, and hydrocarbon setting of the northern margin of South America. In J. L. Pindell, & C. L. Drake (Eds.), Paleogeographic evolution and non-glacial eustasy, northern South America: SEPM (Society for Sedimentary Geology), Special Publication (Vol. 58, pp. 45–85). https://doi.org/10.2110/pec.98.58.0045

Pindell, J. L., & Kennan, L. (2009). Tectonic evolution of the Gulf of Mexico, Caribbean and northern South America in the mantle reference frame: An update. *Geological Society, London, Special Publications*, *328*(1), 1–55. https://doi.org/10.1144/sp328.1

Polonia, A., Torelli, L., Artoni, A., Carlini, M., Faccenna, C., Ferranti, L., et al. (2016). The Ionian and Alfeo-Etna fault zones: New segments of an evolving plate boundary in the central Mediterranean Sea? *Tectonophysics*, *675*, 69–90. https://doi.org/10.1016/j.tecto.2016.03.016

Prentice, C. S., Weber, J. C., Crosby, C. J., & Ragona, D. (2010). Prehistoric earthquakes on the Caribbean–South American plate boundary, Central Range fault, Trinidad. *Geology*, *38*(8), 675–678. https://doi.org/10.1130/g30927.1

Reiners, P. W. (2005). Zircon (U–Th)/He thermochronometry. *Reviews in Mineralogy and Geochemistry*, *58*, 151–179. https://doi.org/10.2138/rmg.2005.58.6

Reiners, P. W., & Farley, K. A. (2001). Influence of crystal size on apatite (U–Th)/He thermochronology: An example from the Bighorn Mountains, Wyoming. *Earth and Planetary Science Letters*, *188*(3–4), 413–420. https://doi.org/10.1016/s0012-821x(01)00341-7

Ringerwole, N., Weber, J., Hippolyte, J.-C., Giorgis, S., & Johnson, M. (2011). Fault slip and paleomagnetic analysis of the tectonics of Tobago, West Indies [abstract], Geological Society of America, Annual Meeting, Abstracts with Programs, *43*(5), 622–715.

Ritter, J., & Weber, J. (2007). Geomorphology and Quaternary geology of the Northern Range, Trinidad and Paria Peninsula, Venezuela: Recording Quaternary subsidence and uplift associated with a pull-apart basin. Proceedings, Geological Society of Trinidad and Tobago, Fourth Geological Conference.

Robertson, P., & Burke, K. (1989). Evolution of the southern Caribbean plate boundary, vicinity of Trinidad and Tobago. *American Association of Petroleum Geologists Bulletin*, *73*, 490–509. https://doi.org/10.1306/44b49fdd-170a-11d7-8645000102c1865d

Roure, F., Carnevali, J. O., Gou, Y., & Subieta, T. (1994). Geometry and kinematics of the North Monagas thrust belt (Venezuela). *Marine and Petroleum Geology*, *11*(3), 347–362. https://doi.org/10.1016/0264-8172(94)90054-x

Russo, R. M., & Speed, R. C. (1992). Oblique collision and tectonic wedging of the South American continent and Caribbean terranes. *Geology*, *20*, 447–450. https://doi.org/10.1130/0091-7613(1992)020<0447:ocatwo>2.3.co;2

Russo, R. M., & Speed, R. C. (1994). Spectral analysis of gravity anomalies and the architecture of tectonic wedging, NE Venezuela and Trinidad. *Tectonics*, *13*(3), 613–622. https://doi.org/10.1029/94tc00052

Russo, R. M., Speed, R. C., Okal, E. A., Shepherd, J. B., & Rowley, K. C. (1993). Seismicity and tectonics of the southeastern Caribbean. *Journal of Geophysical Research*, *98*(B8), 14299–14319. https://doi.org/10.1029/93jb00507

Saunders, J. B. (1972). Recent paleontological results from the northern Range of Trinidad. In C. Petzall (Ed.), *Transactions of the Sixth Caribbean Geological Conference, Margarita, Venezuela* (pp. 455–459).

Soto, D., Mann, P., & Escalona, A. (2011). Miocene-to-recent structure and basinal architecture along the Central Range strike-slip fault zone, eastern offshore Trinidad. *Marine and Petroleum Geology*, *28*(1), 212–234. https://doi.org/10.1016/j.marpetgeo.2010.07.011

Speed, R., Russo, R., Weber, J., & Rowley, K. C. (1991). Evolution of southern Caribbean plate boundary, vicinity of Trinidad and Tobago: Discussion. *The American Association of Petroleum Geologists Bulletin*, *75*(11), 1789–1794. https://doi.org/10.1306/0c9b2a33-1710-11d7-8645000102c1865d

Speed, R. C. (1985). Cenozoic collision of the Lesser Antilles Arc and continental South America and the origin of the El Pilar Fault. *Tectonics*, *4*(1), 41–69. https://doi.org/10.1029/tc004i001p00041

Speed, R. C., Sharp, W. D., & Foland, K. A. (1997). Late Paleozoic granitoid gneisses of northeastern Venezuela and the North America-Gondwana collision zone. *The Journal of Geology*, *105*(4), 457–470. https://doi.org/10.1086/515939

Speed, R. C., & Smith-Horowitz, P. L. (1998). The Tobago Terrane. *International Geology Review*, *40*(9), 805–830. https://doi.org/10.1080/00206819809465240

Summa, L. L., Goodman, E. D., Richardson, M., Norton, I. O., & Green, A. R. (2003). Hydrocarbon systems of Northeastern Venezuela: Plate through molecular scale-analysis of the genesis and evolution of the Eastern Venezuela Basin. *Marine and Petroleum Geology*, *20*(3–4), 323–349. https://doi.org/10.1016/s0264-8172(03)00040-0

Tagami, T., Galbraith, R., Yamada, R., & Laslett, G. (1998). Revised annealing kinetics of fission tracks in zircon and geological implications. In P. Van den Haute, & De Corte (Eds.), *Advances in fission-track geochronology* (pp. 99–112). Kluwer. https://doi.org/10.1007/978-94-015-9133-1_8

Turcotte, D. L., & Schubert, G. (2014). *Geodynamics* (3rd ed.). Cambridge University Press.

van Benthem, S., Govers, R., Spakman, W., & Wortel, R. (2013). Tectonic evolution and mantle structure of the Caribbean. *Journal of Geophysical Research: Solid Earth*, *118*(6), 3019–3036. https://doi.org/10.1002/jgrb.50235

VanDecar, J. C., Russo, R. M., James, D. E., Ambeh, W. B., & Franke, M. (2003). Aseismic continuation of the Lesser Antilles slab beneath continental South America. *Journal of Geophysical Research*, *108*(B1), 2043. https://doi.org/10.1029/2001jb000884

Wadge, G., & Shepherd, J. B. (1984). Segmentation of the Lesser Antilles subduction zone. *Earth and Planetary Science Letters*, *71*(2), 297–304. https://doi.org/10.1016/0012-821x(84)90094-3

Wallace, L. M., Beavan, J., McCaffrey, R., & Darby, D. (2004). Subduction zone coupling and tectonic block rotation in the North Island, New Zealand. *Journal of Geophysical Research*, *109*, B12406. https://doi.org/10.1029/2004JB003241

Weber, J. C. (2005). Neotectonics in the Trinidad and Tobago, West Indies Segment of the Caribbean–South American Plate Boundary. Geological Institute of Hungary, 204(Occasional Papers), 21–29.

Weber, J. C., Dixon, T. H., DeMets, C., Ambeh, W. B., Jansma, P., Mattioli, G., et al. (2001). GPS estimate of relative motion between the Caribbean and South American plates, and geologic implications for Trinidad and Venezuela. *Geology*, *29*(1), 75–78. https://doi.org/10.1130/0091-7613(2001)029<0075:geormb>2.0.co;2

Weber, J. C., Ferrill, D. A., & Roden-Tice, M. K. (2001). Calcite and quartz microstructural geothermometry of low-grade metasedimentary rocks, Northern Range, Trinidad. *Journal of Structural Geology*, *23*(1), 93–112. https://doi.org/10.1016/s0191-8141(00)00066-3

Weber, J. C., Geirsson, H., Latchman, J. L., Shaw, K., La Femina, P., Wdowinski, S., et al. (2015). Tectonic inversion in the Caribbean-South American plate boundary: GPS Geodesy, Seismology, and Tectonics of the Mw 6.7 April 22 1997 Tobago earthquake. *Tectonics*, *34*, 1181–1194. https://doi.org/10.1002/2014tc003665

Weber, J. C., Saleh, J., Balkaransingh, S., Dixon, T., Ambeh, W., Leong, T., et al. (2011). Triangulation-to-GPS and GPS-to-GPS geodesy in Trinidad, West Indies: Neotectonics, seismic risk, and geologic implications. *Marine and Petroleum Geology*, *28*(1), 200–211. https://doi.org/10.1016/j.marpetgeo.2009.07.010

Wortel, R., Govers, R., & Spakman, W. (2009). Continental Collision and the STEP-wise Evolution of Convergent Plate Boundaries: From Structure to Dynamics. In S. Lallemand, & F. Funiciello (Eds.), *Subduction zone geodynamics* (pp. 47–59). Springer Berlin Heidelberg. https://doi.org/10.1007/978-3-540-87974-9_3

Zapata, S., Sobel, E. R., del Papa, C., Jelinek, R., & Glodny, J. (2019). Using a paleosurface to constrain low-temperature thermochronological data: Tectonic evolution of the Cuevas range, Central Andes. *Tectonics*, *38*, 3939–3958. https://doi.org/10.1029/2019TC005887

Zeitler, P., Meltzer, A., Coons, P., Craw, D., Hallet, B., Chamberlin, C. P., et al. (2001). Erosion, Himalayan geodynamics, and the geomorphology of metamorphism. *Geological Society of America Today*, *1*, 4–9. https://doi.org/10.1130/1052-5173(2001)011<0004:ehgatg>2.0.co;2

Zeitler, P. K., Meltzer, A. S., Brown, L., Kidd, W. S. F., Lim, C., & Enkelmann, E. (2014). Tectonics and topographic evolution of Namche Barwa and the easternmost Lhasa Block. In J. Nie, G. D. Hoke, & B. Horton (Eds.), Towards an improved understanding of uplift mechanisms and the elevation history of the Tibetan Plateau (Vol. 507, pp. 23–58). Geological Society of America Special Paper. https://doi.org/10.1130/2014.2507(02)